FEATURE ARTICLE

Why Are There so Few Magnetic Ferroelectrics?

Nicola A. Hill

Materials Department, University of California, Santa Barbara, California 93106-5050

Received: January 7, 2000; In Final Form: April 25, 2000

Multiferroic magnetoelectrics are materials that are both ferromagnetic and ferroelectric in the same phase. As a result, they have a spontaneous magnetization that can be switched by an applied magnetic field, a spontaneous polarization that can be switched by an applied electric field, and often some coupling between the two. Very few exist in nature or have been synthesized in the laboratory. In this paper, we explore the fundamental physics behind the scarcity of ferromagnetic ferroelectric coexistence. In addition, we examine the properties of some known magnetically ordered ferroelectric materials. We find that, in general, the transition metal d electrons, which are essential for magnetism, reduce the tendency for off-center ferroelectric distortion. Consequently, an additional electronic or structural driving force must be present for ferromagnetism and ferroelectricity to occur simultaneously.

1. Introduction

The formal study of ferroelectric materials began over a century ago when anomalously large piezoelectric constants were observed in the material known as Rochelle salt.[1] Over the following few decades, hysteresis was reported in the polarization, dielectric function, and strain of this material,[2] and theories emerged to account for its anomalous dielectric, piezoelectric, elastic, and phase transition behaviors.[3] In the 1930s, another group of materials, based on KH_2PO_4, was discovered to be ferroelectric,[4] and a theory of the ferroelectric phase transition was developed.[5] Ferroelectricity was observed in $BaTiO_3$ and related perovskite-structure oxides in the 1940s,[6] stimulating research in both discovery and characterization of ferroelectric materials. There has been a great increase in the understanding of the fundamental physics of ferroelectrics over the last 10 years,[7] which, in turn, has contributed to the optimization of materials for specific device applications. Today, ferroelectrics are used in a range of applications, including transducers and actuators (because of their piezoelectricity), capacitors (because of their high dielectric permittivity), and memory applications (because their hysteresis properties result in two stable states of opposite polarization).

The past few years have also seen a flurry of activity in the study of magnetic materials, which previously (according to a recent article in *Physics Today*) had an image of "musty physics laboratories peopled by old codgers with iron filings under their nails".[8] However advances in atomic- and nanoscale growth and characterization techniques over the past few years have led to the production of modern magnetic materials that reveal a range of fascinating phenomena. These phenomena derive from the fact that electrons have *spin* as well as charge, giving an extra level of complexity to the physics and an extra degree of freedom in device design. Today, the science and technology of magnetism have undergone a renaissance, driven both by the urge to understand the new physics and by demand from industry for better materials.[9]

The potential impact on society of the recent advances in magnetic materials is extensive. Some examples, such as dramatic increases in data storage density, are already evident. The discoveries of giant[10] and colossal[11] magnetoresistive materials, in which magnetic fields cause order of magnitude changes in conductivity, have been particularly significant, and sensors, read heads, and memories based on giant magnetoresistive magnetic multilayers are already commercially available. Other proposed technologies are still under development. These include magnetic valves, which allow current to pass only when adjacent ferromagnetic layers are oriented by an applied magnetic field, and spin transistors,[12] in which spin-polarized currents are biased and controlled by magnetic rather than electric fields. In addition, the long relaxation times and persistent coherence of electron spins are being investigated for use in quantum computing.[13]

This paper explores a somewhat obscure class of materials known as magnetoelectric multiferroics, which are simultaneously ferroelectric *and* ferromagnetic (or at least show some kind of magnetic ordering). Such materials have all the potential applications of both their parent ferroelectric and ferromagnetic materials. In addition, a whole range of new applications can be envisaged.[14] First, the ability to couple to either the electric or the magnetic polarization allows an additional degree of freedom in device design. Other applications include multiple-state memory elements, in which data is stored both in the electric and the magnetic polarizations, or novel memory media, which might allow the writing of a ferroelectric data bit and the reading of the magnetic field generated by association. Aside from the potential applications, the fundamental physics of multiferroic materials is rich and fascinating.

In this work, we focus on one aspect of the physics of multiferroic magnetoelectrics, which is the puzzling question of why so few exist. After briefly reviewing the basics of ferromagnetism and ferroelectricity in sections 2 and 3, we discuss the history and properties of multiferroic materials in
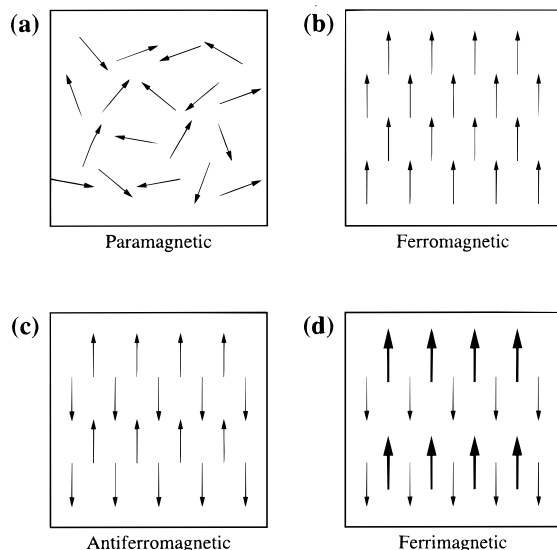
Feature Article

J. Phys. Chem. B, Vol. 104, No. 29, 2000 **6695**

Figure 1. Ordering of the magnetic dipoles in magnetic materials.

Figure 2. Hysteresis loop for a ferro- or ferrimagnet.

section 4. In section 5, we describe the properties of two known multiferroic materials—bismuth manganite and yttrium manganite—and present the results of our calculations for determining the origin of the multiferroism in these materials. Finally, in Section 6, we summarize our results and suggest some potential avenues for the exploration of new multiferroic materials. The computational techniques used in this work are described in the Appendix.

2. Ferromagnets (and Other Magnetic Materials)

A ferromagnetic material is one that undergoes a phase transition from a high-temperature phase that does not have a macroscopic magnetic moment to a low-temperature phase that has a spontaneous magnetization even in the absence of an applied magnetic field. The macroscopic magnetization is caused by the magnetic dipole moments of the atoms (which are aligned randomly in the high-temperature paramagnetic phase, Figure 1a) tending to line up in the same direction, as shown in Figure 1b. The spontaneous magnetization means that ferromagnetic materials tend to concentrate magnetic flux density (they have a large positive permeability), which leads to their widespread use in applications such as transformer cores, permanent magnets, and electromagnets, for which large magnetic fields are required.

As-prepared samples of ferromagnets often lack a macroscopic magnetization because of the presence of *domains* of magnetization oriented in different directions. The subsequent alignment and reorientation of the domains upon the application of a magnetic field, **H**, results in a hysteresis in the magnetization and flux density, **B**, as shown in Figure 2. The ferromagnetic material starts in an unmagnetized state, and as the field is increased in the positive direction, the magnetic induction increases from zero to the saturation induction, $\mathbf{B_s}$. When the field is reduced to zero *after* saturation, the induction decreases from $\mathbf{B_s}$ to $\mathbf{B_r}$, the *residual induction*, or retentivity. The reversed field required to reduce the induction to zero is called the *coercivity*, $\mathbf{H_c}$.

The suitability of ferromagnetic materials for particular applications is determined largely from characteristics shown by their hysteresis loops. For example, a square-shaped hysteresis loop, with two stable magnetization states, is suitable for magnetic data storage, whereas a small hysteresis loop that is easily cycled between states is suitable for a transformer core with a rapidly switching field direction.
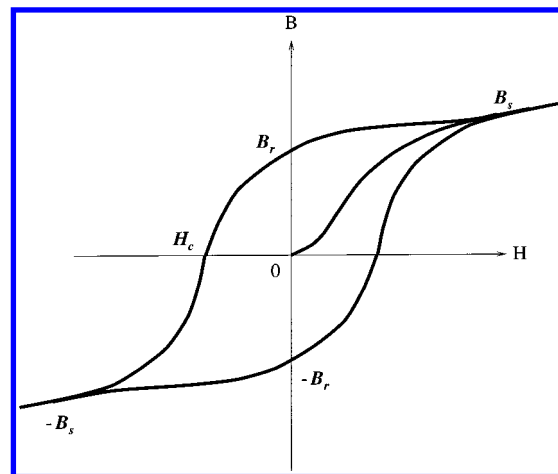
Although ferromagnetic ferroelectric materials are the focus of this work, we will also consider ferroelectric materials displaying other types of magnetic ordering such as antiferromagnetism, ferrimagnetism, or weak ferromagnetism. In antiferromagnetic materials, the constituent atoms or ions have magnetic dipole moments that are ordered antiparallel to each other (Figure 1c). Antiferromagnets do not find wide application in magnetic technologies because they do not have a net overall magnetization. Ferrimagnets are somewhat like antiferromagnets, in that the dipoles align antiparallel; however, some of the dipole moments are larger than others, so the material has a net overall magnetic moment. As a result, ferrimagnets, like ferromagnets, tend to concentrate magnetic flux in their interiors and, therefore, to have wide applicability. The term "weak ferromagnetism" is used to describe antiferromagnets with a small canting of the spins away from antiparallel alignment. This results in a small net magnetization, usually at low temperature.

2.1. Theories of Ferromagnetism: What Makes Ferromagnets Ferromagnetic? There are two phenomenological theories of ferromagnetism that have been successful in explaining many of the properties of ferromagnets: the Curie–Weiss localized-moment theory and the Stoner band theory of ferromagnetism.

In a classic 1907 paper,[15] Weiss postulated that an internal "molecular field" acts in ferromagnetic materials to align the magnetic moments parallel to each other. We now understand the origin of this molecular field to be the quantum mechanical exchange energy, which causes electrons with parallel spins (and therefore parallel magnetic moments) to have a lower energy than electrons with antiparallel spins, all other factors being equal. Below the Curie temperature, T_c, the molecular field is so strong that it magnetizes the substance even in the absence of an external applied field. At high enough temperatures, the thermal energy, kT, is larger than the alignment energy of the molecular field, resulting in the random orientation of the magnetic moments and paramagnetic behavior. The Weiss localized-moment picture explains the experimentally observed Curie–Weiss law behavior for the susceptibility, χ, of many magnetic materials, namely

$$\chi = \frac{C}{T - T_c} \tag{1}$$

There is a divergence in the magnetic susceptibility at the Curie temperature when the magnetic moments align spontaneously even in the absence of an applied magnetic field. The suscep-
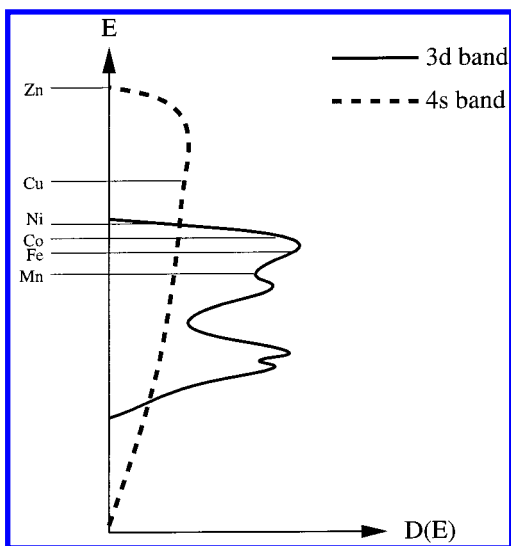
Figure 3. Schematic 3d and 4s densities of states, $D(E)$, in first-row transition metals. The horizontal lines show the positions of the Fermi levels in Zn, Cu, Ni, Co, Fe, and Mn.

Figure 4. 3d and 4s up- and down-spin densities of states in first-row transition metals, with exchange interaction included.

tibility of many antiferromagnets and ferrimagnets is also well described within the localized-moment picture.

The Weiss localized-moment theory breaks down in one important aspect however: it is unable to account for the measured values of the magnetic moment per atom in some ferromagnetic materials, particularly in ferromagnetic metals. There are two significant discrepancies. First, according to the Weiss theory, the magnetic dipole moment on each atom or ion should be the same in both the ferromagnetic and paramagnetic phases. Experimentally this is not the case. Second, in the localized-moment theory, the magnetic dipole moment on each atom or ion should correspond to an integer number of electrons. Again, this is not observed experimentally. To explain these data we need to use the Stoner band theory of ferromagnetism.

In the Stoner theory,[16] the fundamental driving force for ferromagnetism is again the exchange energy, which is minimized if all of the electrons have the same spin. Opposing the alignment of spins is the increased band energy involved in transferring electrons from the lowest band states (occupied equally with up- and down-spin electrons) to band states of higher energy. This band energy prevents simple metals from being ferromagnetic.

In the elemental ferromagnetic transition metals Fe, Ni, and Co, the Fermi energy lies in a region of overlapping 3d and 4s bands, as shown schematically in Figure 3. As a result of the overlap between the 4s and 3d bands, the valence electrons partially occupy both the 3d and 4s bands. For example, Ni, with 10 valence electrons per atom, has 9.46 electrons in the 3d bands and 0.54 electrons in the 4s bands. The 4s bands are broad, with a low density of states at the Fermi level. Consequently, the energy that would be required to promote a 4s electron into a vacant state so that it could reverse its spin is more than the energy that would be gained by the resulting decrease in exchange energy. In contrast, the 3d band is narrow and has a much higher density of states at the Fermi level. The large number of electrons near the Fermi level reduces the band energy required to reverse a spin, and the exchange effect dominates.

It is useful to picture the exchange interaction as shifting the energy of the 3d band for electrons with one spin direction relative to the band for electrons with the opposite spin direction.
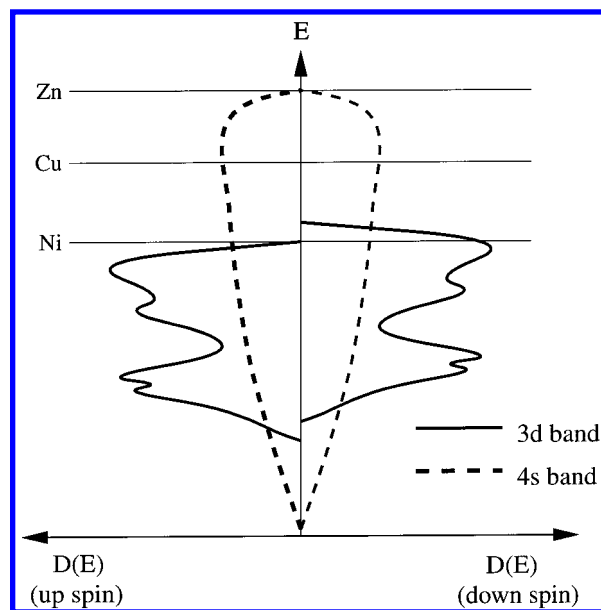
Figure 4 shows the 4s and 3d densities of states within this picture. The magnitude of the shift is independent of the wavevector, giving a rigid displacement of the states in a band with one spin direction relative to the states with the opposite spin direction. If the Fermi energy lies within the 3d band, then the displacement will lead to more electrons of the lower-energy spin direction and, hence, a spontaneous magnetic moment in the ground state. In Ni, for example, the exchange interaction displacement is so strong that one 3d subband is filled with five electrons, and the other contains all 0.54 holes. Thus, the saturation magnetization of Ni is $M = 0.54N\mu_B$, where N is the total number of Ni atoms in the sample. We now see why the magnetic moments of the transition metals do not correspond to integer numbers of electrons! This model also explains why the later transition metals, Cu and Zn, are not ferromagnetic. In Cu, the Fermi level lies *above* the 3d bands. Because both of the 3d bands are filled and the 4s band has no exchange splitting, the numbers of up- and down- spin electrons are equal. In Zn, both the 3d and 4s bands are filled and so do not contribute a magnetic moment.

3. Ferroelectrics

The formal definition of a ferroelectric material is one that undergoes a phase transition from a high-temperature phase that behaves as an ordinary dielectric (so that an applied electric field induces an electric polarization, which goes to zero when the field is removed) to a low-temperature phase that has a spontaneous polarization whose direction can be switched by an applied field. Many properties of ferroelectric materials are analogous to those of ferromagnets, but with the electric polarization, **P**, corresponding to the magnetization, **M**; the electric field, **E**, corresponding to the magnetic field, **H**; and the electric displacement, **D**, corresponding to the magnetic flux density, **B**.

For example, ferroelectric materials also have domains and show a hysteretic response of both polarization and electric displacement to an applied electric field. As a result, they also find applications in data storage. The onset of spontaneous *electric* polarization coincides with a divergence in the static *dielectric* permeability, ϵ, because at T_c, an infinitesimally small external electric field will cause a large polarization. They find

Feature Article

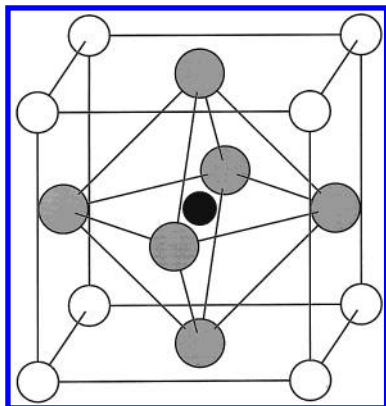*J. Phys. Chem. B, Vol. 104, No. 29, 2000* **6697**

Figure 5. Cubic perovskite structure. The small B cation (in black) is at the center of an octahedron of oxygen anions (in gray). The large A cations (white) occupy the unit cell corners.

application as capacitors because their concentration of *electric* flux density results in high dielectric permeabilities. They are also used in electromechanical transducers and actuators (because the change in electric polarization is accompanied by a change in shape.[17])

Early work on ferroelectric materials[1,2] focused primarily on Rochelle salt, $KNa(C_4H_4O_6) \cdot 4H_2O$. Although studies of Rochelle salt were pivotal in establishing many of the basic properties of ferroelectric materials, the complex structure and large number of ions per unit cell made it difficult to elucidate a coherent theory of ferroelectricity from the results of experiments on this material. The most widely studied and widely used ferroelectrics today are perovskite-structure oxides, ABO_3, which have the prototypical cubic structure shown in Figure 5. The cubic perovskite structure is characterized by a small cation, B, at the center of an octahedron of oxygen anions, with large cations, A, at the unit cell corners. Below the Curie temperature, there is a structural distortion to a lower-symmetry phase accompanied by the shift off-center of the small cation. The spontaneous polarization derives largely from the electric dipole moment created by this shift. The comparatively simple perovskite structure and the small number of atoms per unit cell have made detailed theoretical studies of perovskite ferroelectrics possible and resulted in a good understanding of the fundamentals of ferroelectricity.

3.1. Theories of Ferroelectricity: What Makes Ferroelectrics Ferroelectric? Any lattice of oppositely signed point charges is inherently unstable. Ionic materials are stable because of short-range repulsions between adjacent electron clouds. The existence or absence of ferroelectricity is determined by a *balance* between these short-range repulsions, which favor the nonferroelectric symmetric structure, and additional bonding considerations, which might stabilize the ferroelectric phase. Even in ferroelectric materials, the short-range repulsions dominate at high temperature, resulting in the symmetric, unpolarized state. As the temperature is decreased, the stabilizing forces associated with the polarization of the ions as they are displaced become stronger than the short-range repulsive ion—ion interactions, and the polarized state becomes stable, even in the absence of an applied field.

First-principles density functional theory calculations have contributed significantly to our current understanding of the origin of ferroelectric behavior, particularly in perovskite-structure oxides. The developments over the last 10 years are described in detail in ref 7; here, we summarize the important results. In 1992, Cohen and Krakauer[18] used density functional theory (DFT) within the local density approximation (LDA) to
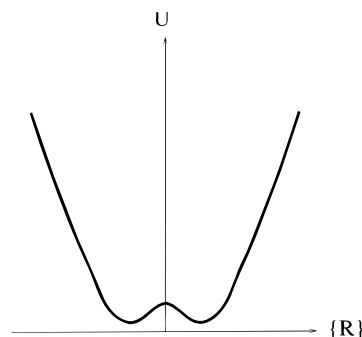

Figure 6. Characteristic double-well potential energy as a function of the position of the B cation between the oxygen anions in perovskite ferroelectrics.

investigate the ferroelectricity in two related perovskite-structure compounds: $PbTiO_3$ and $BaTiO_3$. Both materials have the cubic structure at high temperatures. $PbTiO_3$ undergoes a phase transition to a tetragonal phase below 766 K, with the polarization along the [100] direction. $BaTiO_3$ undergoes a series of phase transitions from cubic to tetragonal to orthorhombic to rhombohedral, with the low-temperature polarization along the [111] direction. Cohen and Krakauer found that, in both cases, the Ti 3d—O 2p hybridization is essential for stabilizing the ferroelectric distortion. In $BaTiO_3$, the Ba—O interaction is largely ionic in nature. In $PbTiO_3$, there is hybridization between the Pb 6s and O 2p electrons. This results in a large Pb polarizability and a strain that stabilizes the tetragonal phase over the rhombohedral phase in $PbTiO_3$.

Two complementary phenomenological models exist for describing the phase transition to the ferroelectric state. The small B cation in ferroelectric perovskite oxides should always be able to lower its energy by shifting along one of the ⟨111⟩ directions (unless strain in the lattice stabilizes a different displacement). This leads to the characteristic "double-well" potential energy for the position of the small cation as a function of position between the oxygen anions, as shown in Figure 6. In the order—disorder model, the B cations are *always* displaced along one of the cube diagonals. At high temperature, all possible ⟨111⟩ directions are allowed, and at low temperature, the displacements all adopt either the same orientation (giving rhombohedral symmetry) or two or three preferred ⟨111⟩ directions (giving tetragonal or orthorhombic symmetry). This model predicts a large change in configurational entropy at the phase transition, which is not in fact observed, but the model may be applicable in higher-temperature regimes, away from the phase transition temperature. In the soft-mode model, the B cation displacement is stable only at low temperatures. Above the Curie temperature, there is a restoring force that tends to push the B cation back to the center if it is displaced. As the temperature is reduced, the phonon associated with this restoring force (the so-called "soft-mode" phonon) becomes weaker, until at the Curie temperature, the frequency is zero and the displacement occurs spontaneously.

The large effect from changing the identity of the A cation is significant for our later discussion of multiferroic materials. The strain introduced by the A cation hybridization with O 2p electrons is long-range in nature and helps lead to the long-range ordering required for a phase transition. Therefore, the identity of the A cation can significantly affect the ferroelectricity of the material, even though the ferroelectric polarization results primarily from the displacement of the B cation relative to the oxygen cage. Also significant is the observation that the Ti^{4+} ion is formally in a d^0 state so that the lowest unoccupied

energy levels are d states that tend to hybridize with O 2p ions. Most other perovskite ferroelectrics also contain d^0 B cations, such as Zr^{4+} and Nb^{5+}. In contrast, d-orbital occupancy is a requirement for the existence of magnetic moments and the consequent existence of magnetic ordering.

4. Multiferroism

The term multiferroism has been coined[19] to describe materials in which two or all three of the properties ferroelectricity, ferromagnetism, and ferroelasticity occur in the same phase. This means that they have a spontaneous magnetization that can be reoriented by an applied magnetic field, a spontaneous polarization that can be reoriented by an applied electric field, and a spontaneous deformation that can be reoriented by an applied stress. Specific device applications that have been suggested for such "multiferroic" materials[14] include multiple-state memory elements, electric-field-controlled ferromagnetic resonance devices, and transducers with magnetically modulated piezoelectricity. In addition, the ability to couple with *either* the magnetic *or* the electric polarization offers an extra degree of freedom in the design of conventional actuators, transducers, and storage devices. In this work, we focus on magnetoelectric multiferroics, which are simultaneously ferromagnetic and ferroelectric, with or without ferroelasticity.

4.1. History of Magnetoelectric Multiferroics. *4.1.1. Boracites.* The first ferromagnetic ferroelectric material to be discovered[20] was nickel iodine boracite, $Ni_3B_7O_{13}I$. This was followed by the synthesis of many more multiferroic boracite compounds, all of which have complex structures with many atoms per formula unit and more than one formula unit per unit cell. The large number of inter-ionic interactions in these materials prevented the isolation both of the essential factors causing multiferroicity and of the nature of the coupling between the magnetic, electric polarization, and structural order parameters. Nickel iodine boracite can be thought of as the "Rochelle salt" of magnetic ferroelectrics—invaluable for demonstrating proof of concept, but unlikely to find wide applicability or to contribute to our increased understanding in the field.

4.1.2. Mixed Perovskites. The search for other ferromagnetic ferroelectrics began in Russia in the 1950s, with the replacement of some of the d^0 B cations in ferroelectric perovskite oxides by magnetic d^n cations.[21] The first synthetic ferromagnetic ferroelectric material, $(1-x)Pb(Fe_{2/3}W_{1/3})O_3 - xPb(Mg_{1/2}W_{1/2})O_3$, was produced in the early 1960s using this approach.[22] Here, the Mg and W ions are diamagnetic and cause the ferroelectricity, and the formally d^5 Fe^{3+} ion is responsible for the magnetic ordering. Other examples include B-site-ordered Pb_2-$(CoW)O_6$,[23] which is ferroelectric and ferromagnetic; B-site disordered $Pb_2(FeTa)O_6$,[23] which is ferroelectric and antiferromagnetic; and $Pb_2(FeTa)O_6$[24] and $Pb_2(FeTa)O_6$,[25] which are both ferroelectric and antiferromagnetic, with weak ferromagnetism below around 10K. As a result of dilution of the magnetic ions, these materials all have rather low Curie or Néel temperatures.

4.1.3. Other Perovskites. A number of other perovskite materials are known to have ferroelectric and magnetic (mostly of the antiferromagnetic type) ordering. These include the manganites of the small rare earth elements and yttrium and a few compounds in which Bi is the large cation. These materials will be discussed in detail in section 5.

4.2. Requirements for Magnetoelectric Multiferroicity. By definition, for a material to be a magnetoelectric multiferroic, it must be simultaneously ferromagnetic and ferroelectric. Therefore, its allowed physical, structural, and electronic properties are restricted to those that occur both in ferromagnetic and in ferroelectric materials. In this section, we analyze a range of properties and discuss how these properties limit our choice of potential materials. We discuss those that are the limiting factors in preventing the simultaneous existence of ferromagnetism and ferroelectricity.

4.2.1. Symmetry. A primary requirement for the existence of ferroelectricity is a structural distortion from the prototypical high-symmetry phase that removes the center of symmetry and allows an electric polarization. There are 31 point groups that allow a spontaneous electric polarization, **P**, and 31 that allow a spontaneous magnetic polarization, **M**.[19] Thirteen point groups $(1, 2, 2', m, m', 3, 3m', 4, 4m'm', m'm2', m'm'2', 6,$ and $6m'm')$ are found in both sets, allowing both properties to exist in the same phase. Although this represents a considerable reduction from the total number of possible crystal structures (the total number of Shubnikov point groups is 122), it is not an insignificant number, and many candidate materials that are *not* in fact ferromagnetic and ferroelectric exist in one of the allowed symmetries. Therefore, it is unlikely that symmetry considerations are responsible for the scarcity of ferromagnetic ferroelectric materials.

4.2.2. Electrical Properties. By definition, a ferroelectric material must be an insulator (otherwise, an applied electric field would inducing an electric current to flow, rather than causing an electrical polarization.) Ferromagnets, although not required to have specific electrical properties, are often metals. For example, the driving force for ferromagnetism in the elemental ferromagnets Fe, Co, and Ni and their alloys is the high density of states at the Fermi level, which also, of course, results in metallicity. Therefore, one could assume that the lack of the simultaneous occurrence of magnetic and ferroelectric ordering is simply the result of a dearth of magnetic insulators. However, if we extend our search to include ferrimagnets or weak ferromagnets (which have canted antiferromagnetic ordering, resulting in a weak magnetic moment in the direction of the canting), this argument no longer holds, because most ferrimagnets or weak ferromagnets are, in fact, insulators. In addition, there are also very few antiferromagnetic ferroelectrics, even though antiferromagnets are usually insulating materials. Therefore, it appears that we cannot blame the lack of magnetically ordered ferroelectrics simply on a shortage of magnetically ordered insulators.

4.2.3. Chemistry:"d^0-ness". We noted in section 3.1 that the common perovskite oxide ferroelectric materials have a formal charge corresponding to the d^0 electron configuration on the B cation. Clearly, if there are no d electrons creating localized magnetic moments, then there can be no magnetic ordering of any type, either ferro-, ferri-, or antiferromagnetic. It appears however that, in most cases, as soon as the d shell on the small cation is partially occupied, the tendency for it to make a distortion that removes the center of symmetry is eliminated. This could be the result of a number of effects, including size, the tendency to undergo a different, more dominant distortion, electronic properties, magnetic properties, or some combination of the above. We now consider the likely influence of each of these factors.

Size of the Small Cation. Are transition metal ions with occupied d shells simply too large to move away from the large space at the center of the oxygen octahedron? In this section, we compare the ionic radii of typical d^0 cations in perovskite ferroelectrics with those of typical d^n cations in nonferroelectric perovskite oxides to see if this argument is correct.

The Shannon ionic radii[26] of some common d^0 small cations found in ferroelectric perovskite oxides are: Ti^{4+}, 74.5 pm;

Feature Article

J. Phys. Chem. B, Vol. 104, No. 29, 2000 **6699**

Nb^{5+}, 78 pm; and Zr^{4+}, 86 pm. Some representative d^n cations that are found as the small cations in *nonferroelectric* perovskite oxides include Mn^{3+} (d^4), Ti^{3+} (d^1), and V^{4+} (d^1) with radii of 78.5, 81, and 72 pm, respectively. Therefore, typical B-site cations with d electron occupation do not have systematically larger radii than typical d^0 B-site cations. We conclude that the size of the B cation is not the deciding factor in the existence or otherwise of ferroelectricity.

Structural Distortions. Ferroelectric materials must undergo a phase transition to a low-temperature phase that does not have a center of symmetry. This is most often achieved in conventional perovskite ferroelectrics by an off-center displacement of the small (B) cation from the center of the oxygen octahedron. However, for cations with certain d-orbital occupancies, the tendency to undergo a Jahn–Teller distortion is strong and will likely be the dominant structural effect. The Jahn–Teller distorted structure might have a lower driving force for off-center displacement than the otherwise undistorted structure.

Examples of this effect are seen in lanthanum manganite, $LaMnO_3$, in which the Mn^{3+} ion has a d^4 configuration, and yttrium titanate, $YTiO_3$, in which the Ti^{3+} ion is d^1. Both materials have a d-type Jahn–Teller distortion, in which the elongated axes of the oxygen octahedra are oriented parallel to each other along the crystallographic c axis.[27] Orbital ordering is observed to occur simultaneously with the Jahn–Teller ordering.[27] $LaMnO_3$ is insulating and an A-type antiferromagnet, in which planes of ferromagnetically aligned Mn^{3+} ions are aligned antiparallel to each other. $YTiO_3$ is a strongly correlated ferromagnetic Mott–Hubbard insulator. Neither material is ferroelectric.

Note the relevance of the *formal* charge on the B cation here. In $BaTiO_3$, the actual occupation of the 3d electrons is closer to d^1 than to d^0 because of donation of charge density from the oxygen ligands.[18] A d^1 cation should undergo a Jahn–Teller distortion. No Jahn–Teller distortion is observed in $BaTiO_3$ however, which is consistent with the d^0 formal charge.

Magnetism versus d-Orbital Occupancy. It is clear that the existence of d electrons on the B-site cation reduces the tendency of perovskite structure oxides to display ferroelectricity. However, it is not clear whether it is merely the presence of d electron density or the influence of the magnetic spin polarization that is the dominant factor in creating this effect. Using first-principles density functional theory calculations, it is possible to answer this question by artificially removing the spin polarization in materials that are experimentally found to be magnetic and determining whether they then become ferroelectric. In sections 5.1 and 5.2, we perform such comparisons for some representative systems and show that removal of the magnetic polarization does not significantly affect the calculated phonon frequencies, suggesting that d-orbital occupancy, rather than d-electron magnetism, is dominant in overriding the tendency to undergo ferroelectric distortion.

4.2.4. Conclusion. The short answer to the title of the paper is that we do not know for sure why there are so few magnetic ferroelectrics. We do, however, have some clues: multiferroism involves a number of subtle competing factors, with d-electron occupancy on the transition metal being a critical variable. In the next section, we present detailed theoretical studies of two known magnetoelectric multiferroic materials with the goal of understanding what makes these particular materials multiferroic. First, we consider bismuth manganite, $BiMnO_3$, which is ferromagnetic and possibly ferroelectric. Second, we study yttrium manganite, $YMnO_3$, which is known to be antiferromagnetic and ferroelectric.

5. Perovskite-Structure Manganites

As we discussed in section 3.1, first-principles studies of perovskite ferroelectrics contributed greatly to our understanding of the fundamentals of ferroelectricity. Similar investigation of *multiferroic* perovskites should allow us to isolate the essentials of multiferroism. In this section, we focus on one specific class of magnetic perovskites—the rare earth (and related) manganites.

A large amount of recent research activity[28] has been focused on the rare earth manganites, following the observation of colossal magnetoresistance (CMR) in Ca-doped $LaMnO_3$.[11] During these recent studies, many rare earth perovskite manganites have been found to show strong coupling between their magnetic and structural order parameters. For example, a magnetically induced structural phase transition has been observed in $La_{0.83}Sr_{0.17}MnO_3$,[29] indicating strong coupling between the local magnetic spin moments and the lattice structure. In $Nd_{0.5}Sr_{0.5}MnO_3$, strong coupling between the magnetic spin moments and the electronic charge carriers was demonstrated when an electronic metal–insulator transition was induced by an external magnetic field.[30] The large change in conductivity with applied magnetic field, which gives these materials potential technological importance as the read element in magnetic recording heads,[31] is believed to originate from a similar type of phase transition.[32] It is clear that, although the combination of ferromagnetism and ferroelectricity is rare, *coupling* between electric and magnetic order parameters is not.

All of the rare earth manganites crystallize in the perovskite phase with antiferromagnetic ordering between adjacent Mn^{3+} ions, caused by the superexchange mechanism.[33] Manganites of the lighter rare earths ($LaMnO_3$ through $DyMnO_3$) have a low-temperature orthorhombic distortion and do not show ferroelectricity. In $YMnO_3$, and in $HoMnO_3$ through $LuMnO_3$, the orthorhombic phase is not the most stable structure, and instead, a hexagonal perovskite structure is formed. The hexagonal manganites are ferroelectric.[34] Bismuth manganite differs markedly from both the orthorhombic and hexagonal rare earth manganites. Although information about $BiMnO_3$ is sparse,[35] it is known to be ferromagnetic, with a triclinic structural distortion in its ground state. The ferromagnetism is unexpected, because, like the rare earth manganites, $BiMnO_3$ has trivalent Mn cations with four 3d electrons. The four 3d electrons should, in all cases, drive a Jahn–Teller distortion of the surrounding oxygen octahedra, which, combined with the superexchange interaction, should cause antiferromagnetic magnetic symmetry,[33] as is indeed observed in the rare earth manganites. In addition, preliminary theoretical work has confirmed an early suggestion[35] that $BiMnO_3$ might be ferroelectric.[36]

In this section, we study the chemical origins of the differences between $BiMnO_3$ and the rare earth manganites and between the hexagonal and orthorhombic manganites. We choose $LaMnO_3$ as our prototypical orthorhombic rare earth manganite and $YMnO_3$ as our prototypical hexagonal manganite. The motivations for our choices are two-fold. First, the majority of the recent experimental data on orthorhombic and hexagonal manganites has been obtained for $LaMnO_3$ and $YMnO_3$, respectively. Second, because La^{3+} and Y^{3+} do not contain f electrons, we are able to use a plane-wave pseudopotential implementation of density functional theory, without the complication of developing pseudopotentials for tightly bound f electrons.

The goal of our computational work in this section is to identify the factors that promote ferroelectricity in $BiMnO_3$ and $YMnO_3$, but override it in the conventional cubic rare earth
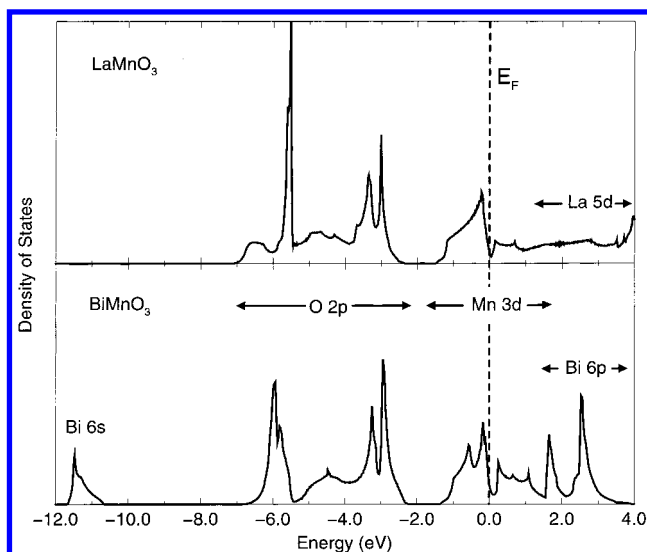
Figure 7. Calculated densities of states for cubic paramagnetic LaMnO$_3$ and BiMnO$_3$.

manganites. In particular, we study the effect of artificially removing the magnetic interactions on the d electrons (by restricting the up- and down-spin charge densities to be identical). This allows us to determine whether it is the magnetism or the d-orbital occupation that prevents the ferroelectric instabilities from being unstable in the perovskite manganites. The theoretical methods and computational details used in this work are described in the Appendix.

5.1. Bismuth Manganite. In this section, we investigate the origin of the differences between ferroelectric BiMnO$_3$ and the nonferroelectric rare earth manganites by comparing the calculated electronic properties of BiMnO$_3$ with those of LaMnO$_3$. We begin by calculating the electronic structure for the high-symmetry cubic phases, without including magnetic effects [the so-called paramagnetic (PM) phase], and then lower the magnetic symmetry to the ferromagnetic (FM) phase. Finally, we introduce structural distortions in both paramagnetic and ferromagnetic calculations. This ability to isolate structural and magnetic distortions is unique to computational studies and allows for an identification of the essential microscopic interactions that cause the observed macroscopic behavior. There are two important questions to answer here. First, why is BiMnO$_3$ ferromagnetic, when the superexchange mechanism causes the other rare earth manganites to be antiferromagnetic? Second, what causes BiMnO$_3$ to be ferroelectric, when the other cubic rare earth manganites do not show a ferroelectric distortion?

5.1.1. Cubic Paramagnetic Structures. Figure 7 shows the calculated densities of states for cubic paramagnetic LaMnO$_3$ and BiMnO$_3$. The plotted energy range is from −12 eV to 4 eV, and the lower-lying semi-core states have been omitted for clarity. The Fermi level is set to zero in both cases. The broad series of bands between −2 and −7 eV in both materials arises from the oxygen 2p orbitals. Above the oxygen 2p bands, and separated from them by an energy gap, are the Mn 3d bands. The Mn 3d bands are divided into two subbands—the lower-energy t_{2g} bands and the higher energy e_g bands—as a result of crystal-field splitting by the octahedral oxygen anions. In both cases, the Fermi level lies near the top of the Mn 3d t_{2g} bands and is in a region of high density of states (DOS). The large DOS at the Fermi level suggests that the cubic PM structure is unstable and that a lower-energy structure could be achieved by allowing spin-polarization and/or structural distortion. One striking *difference* between the two DOS plots is the presence
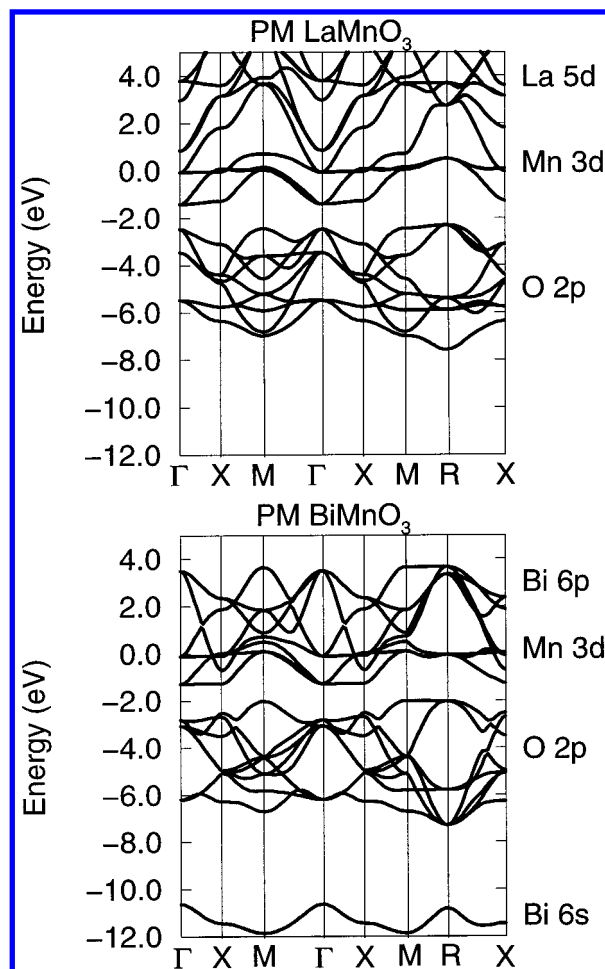

Figure 8. Calculated band structures for cubic paramagnetic LaMnO$_3$ and BiMnO$_3$ along the high-symmetry axes of the Brillouin zone.

of a band between −10 and −12 eV in the BiMnO$_3$ band structure that does not exist in the LaMnO$_3$ case. This band corresponds to the high-lying occupied Bi 6s electrons. In addition, the high-energy La 3d electrons have a very different form than the Bi 6p electrons, which occupy a similar energy range.

Figure 8 shows the corresponding band structures along the high-symmetry axes of the simple cubic Brillouin zone. Again, the broad O 2p bands between −2 and −7 eV can be seen clearly in both materials, with the Mn 3d bands above them, separated by an energy gap. Again, we observe the Bi 6s band, which can be seen to have considerable dispersion, suggesting that it is involved in covalent bonding. Note that the Mn 3d bands in BiMnO$_3$ overlap with the partially occupied Bi 6p orbitals, whereas in LaMnO$_3$, the next highest bands are the unoccupied La 5d bands.

The differences between the two band structures show up clearly in the bands along the Γ → X line. This region of the band structure is shown in Figure 9 with the symmetry labels added and the energy scale extended to include the lower energy O 2s and La 5p bands. In the following discussion, we focus on the bands with Δ_1 symmetry as capturing the essential features. The Δ_1 bands are plotted with solid lines, and all other bands with dashed lines in Figure 9.

In LaMnO$_3$, the two oxygen 2p Δ_1 bands decrease monotonically in energy from Γ to X, and the Mn 3d Δ_1 band increases monotonically from Γ to X. Analysis of the charge density shows that the Fermi surface at the Γ point consists largely of Mn 3d electrons, with contributions from other atoms being very small. The charge density at the X point is very similar, except
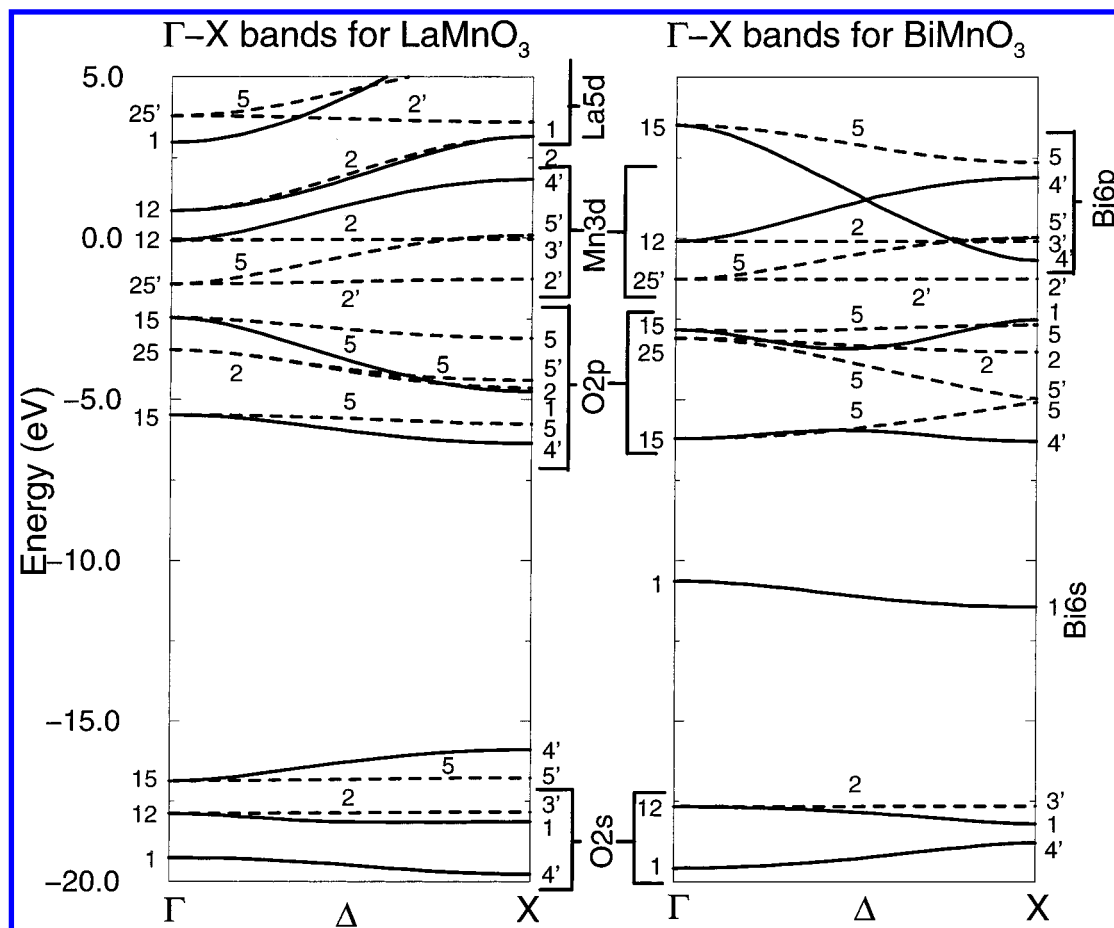
Feature Article

J. Phys. Chem. B, Vol. 104, No. 29, 2000 **6701**

Figure 9. Calculated band structures for cubic paramagnetic LaMnO$_3$ and BiMnO$_3$ along the $\Gamma \rightarrow$ X axis. The solid lines show the bands of Δ_1 symmetry.

that there is a small oxygen contribution, indicating that the amount of Mn 3d–O 2p hybridization increases along the Γ to X line.

In BiMnO$_3$ the behavior is quite different. First, the X$_1$ symmetry of the Bi 6s band at the X point causes the X$_1$ O 2p band to be "pushed up" in energy, resulting in a different ordering of the O 2p bands at the X point. The very dispersive Bi 6p Δ_1 band crosses the Mn 3d Δ_1 band and moves below the Fermi level near the X point. As a result, the charge distribution at the Γ point is similar to that of LaMnO$_3$; however, at X, there is a significant amount of charge density around the Bi atoms. Further analysis reveals that the Bi component is in the X$_4'$ band, which crossed the highest Mn 3d band.

To quantify the differences between cubic PM BiMnO$_3$ and LaMnO$_3$, we performed tight-binding analyses of the Γ to X regions of the respective band structures. Tight-binding parameters were obtained by nonlinear least-squares fitting[37] to the calculated ab initio energies at the high-symmetry Γ and X points and at 19 points along the Δ axis. First, we performed analyses with only oxygen 2s and 2p and Mn 3d orbitals included in the basis set. The tight-binding parameters thus obtained are given in Table 1. The band energies calculated using these parameters have root-mean-square (RMS) deviations from the ab initio energies of 0.20 for LaMnO$_3$ and 0.25 for BiMnO$_3$. The resulting band structures for the bands of Δ_1 symmetry are compared with the ab initio values in Figure 10. The limited basis set reproduces the LaMnO$_3$ bands well, consistent with an early proposal by Goodenough[33] that the magnetic properties of LaMnO$_3$ are determined by the Mn 3d–O 2p hybridization only. Note that the fit to the lower-energy O 2s bands is the least good; these bands are very close in energy

TABLE 1: Tight-Binding Parameters (in eV) for BiMnO$_3$, LaMnO$_3$, and YMnO$_3$[a,b]

	BiMnO$_3$	LaMnO$_3$	YMnO$_3$
E_{O2s}	−17.6806	−17.8364	−17.9649
E_{O2p}	−3.4444	−4.5140	−4.7382
E_{Mn3d}	−1.2024	−1.1913	−1.4097
$V_{O2s-O2s}$	−0.2521	−0.2437	−0.2461
$V_{(O2p-O2p)\sigma}$	0.7352	0.6206	−0.7167
$V_{(O2p-O2p)\pi}$	−0.1322	−0.0635	−0.1069
$[V_{(O2p-O2p)\sigma}]_2$	−0.2119	0.1826	0.1688
$[V_{(O2p-O2p)\pi}]_2$	−0.0448	0.0830	0.0620
$V_{O2s-Mn3d}$	−1.7207	−1.7358	−1.9711
$V_{(O2p-Mn3d)\sigma}$	−1.9642	−1.8385	−2.0601
$V_{(O2p-Mn3d)\pi}$	1.0363	0.8790	1.0837
$V_{(Mn3d-Mn3d)\delta}$	−0.0034	0.0663	0.0488

[a] Parameters obtained by nonlinear least-squares fitting to the ab initio eigenvalues along Γ to X. [b] E indicates an orbital energy, and V, an interatomic transfer integral. All transfer integrals are between nearest neighbors, except those with the subscript "2", which are between next-nearest neighbors. Only the parameters listed in the table were allowed to be nonzero in the fitting procedure.

to the La 5p bands, which have not been included in the fit. The behavior of the BiMnO$_3$ Δ_1 bands is less well reproduced, confirming that additional orbital overlaps are essential in producing the observed band structure.

We then repeated the fitting procedure for BiMnO$_3$, with Bi 6s and 6p orbitals added to the basis. Transfer integrals between nearest-neighbor Bi 6s–O 2p, Bi 6p–O 2p, Bi 6p–Mn 3d, and Bi 6p–Bi 6p orbitals were allowed to be nonzero. This significantly improved the quality of the fit to the ab initio bands (see Figure 11) and reduced the root-mean-square deviation to 0.12. The values of the new tight-binding parameters are given
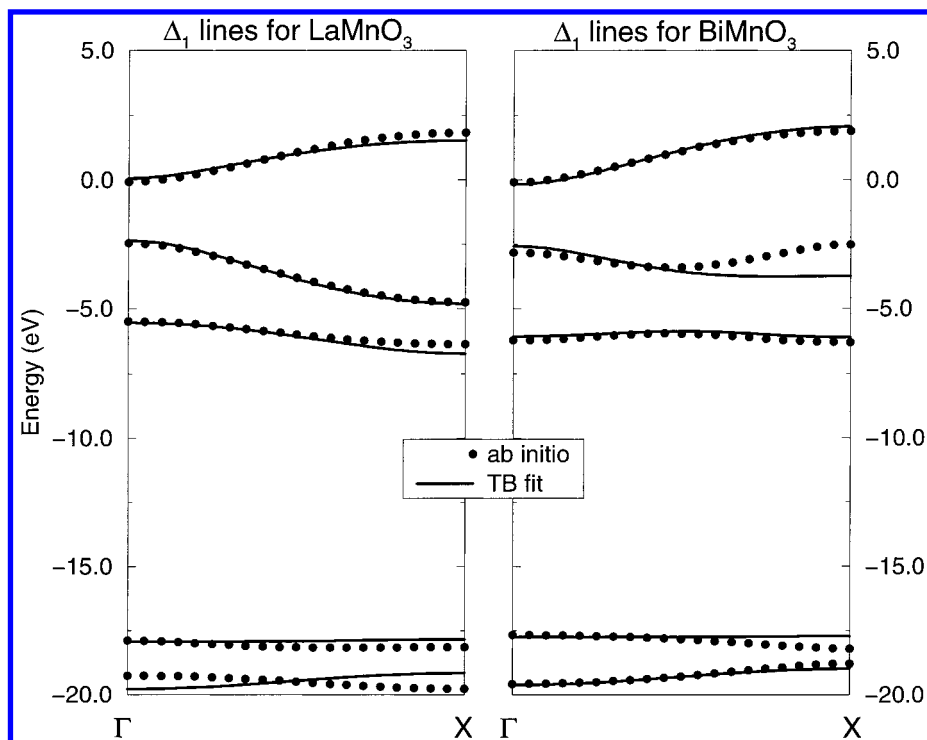
Figure 10. Comparison of ab initio Δ_1 bands with those obtained from a tight-binding fit using only Mn and O orbitals in the basis. The fit for LaMnO$_3$ is good, indicating that only the Mn and O ions are significantly involved in covalent bonding. The fit for BiMnO$_3$ has a higher RMS deviation and, in particular, misses the additional curvature at around -3 eV near the X point. This shows that additional interactions are present.
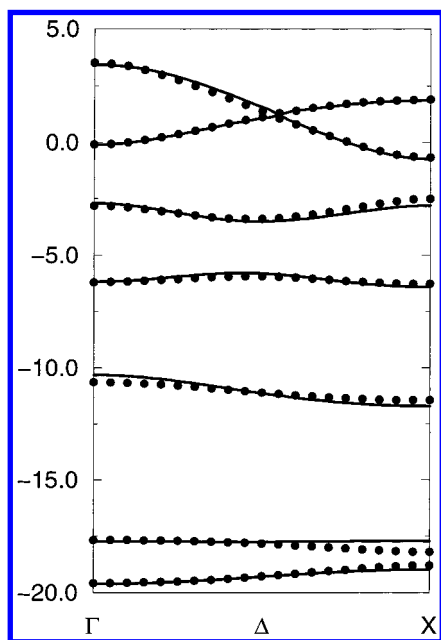

Figure 11. Comparison of ab initio Δ_1 bands with those obtained from a tight-binding fit including Bi 6s and 6p orbitals in addition to Mn 3d and O 2s and 2p. The fit is improved over the fit using only Mn and O orbitals.

TABLE 2: Tight-binding Parameters (in eV) for BiMnO$_3{}^{a,b}$

	BiMnO$_3$		BiMnO$_3$
E_{Bi6s}	-10.310688	$V_{(Bi6p-Mn3d)\pi}$	0.078144
E_{Bi6p}	0.202695	$V_{O2s-O2s}$	-0.237506
E_{O2s}	-17.717958	$V_{(O2p-O2p)\sigma}$	0.652059
E_{O2p}	-3.725773	$V_{(O2p-O2p)\pi}$	-0.125450
E_{Mn3d}	-1.167871	$[V_{(O2p-O2p)\sigma}]_2$	-0.010196
$V_{(Bi6p-Bi6p)\sigma}$	0.848443	$[V_{(O2p-O2p)\pi}]_2$	-0.002797
$V_{(Bi6p-Bi6p)\pi}$	0.166061	$V_{O2s-Mn3d}$	-1.645508
$V_{Bi6s-O2p}$	-0.812502	$V_{(O2p-Mn3d)\sigma}$	-1.926533
$V_{(Bi6p-O2p)\sigma}$	-1.061660	$V_{(O2p-Mn3d)\pi}$	0.959768
$V_{(Bi6p-O2p)\pi}$	-0.145201	$V_{(Mn3d-Mn3d)\delta}$	0.029347
$V_{(Bi6p-Mn3d)\sigma}$	0.170850		

^{a} Parameters obtained by nonlinear least-squares fitting to the ab initio eigenvalues along Γ to X. ^{b} An expanded tight-binding basis including the Bi 6s and 6p orbitals was used. The labeling scheme for the parameters is the same as in Table 1. Only the parameters shown were allowed to be nonzero.

in Table 2. The largest transfer integrals involving Bi are the Bi 6s$-$O 2p and Bi 6p$-$O 2p σ interactions, with the magnitude of the σ-bonded Bi 6p$-$O 2p interaction being approximately 30% larger than that of the Bi 6s$-$O 2p. Also large are the Bi 6p$-$Bi 6p σ interactions, which cause the Bi 6p Δ_1 band to be pushed down below the Fermi level.

5.1.2. Preliminary Experimental Results for BiMnO$_3$. The conclusion from our tight-binding analysis, that there is strong hybridization between the O 2p and Bi 6p orbitals, is consistent with recent measurements showing an enhancement of charge

ordering in Bi-doped CaMnO$_3$.[38] Cheetham and co-workers observed that the charge-ordered state in Bi$_{0.3}$Ca$_{0.7}$MnO$_3$ persists to a higher temperature than does the charge-ordered state in La$_{0.3}$Ca$_{0.7}$MnO$_3$. They explained their observations by noting that the electronegativity of Bi enhances Bi$-$O hybridization and, in turn, reduces the amount of Mn$-$O hybridization. This also provides a plausible explanation for the existence of ferromagnetism in BiMnO$_3$. The combination of structural distortion and reduced Mn 3d$-$O 2p overlap (both driven by bismuth$-$oxygen covalency) reduces the strength of the anti-ferromagnetic superexchange interaction, making ferromagnetic coupling more favorable.

Additional evidence in support of this phenomenon can be extracted from ref 39, in which a temperature$-$composition phase diagram for Bi$_{1-x}$Ca$_x$MnO$_3$, showing the charge-ordered transition and the Néel temperature, is plotted. Comparison with similar data for La$_{1-x}$Ca$_x$MnO$_3$ (for example, in ref 40) confirms that the charge-ordered phase persists to higher temperature in Bi-doped CaMnO$_3$ than in La-doped CaMnO$_3$. Therefore, in
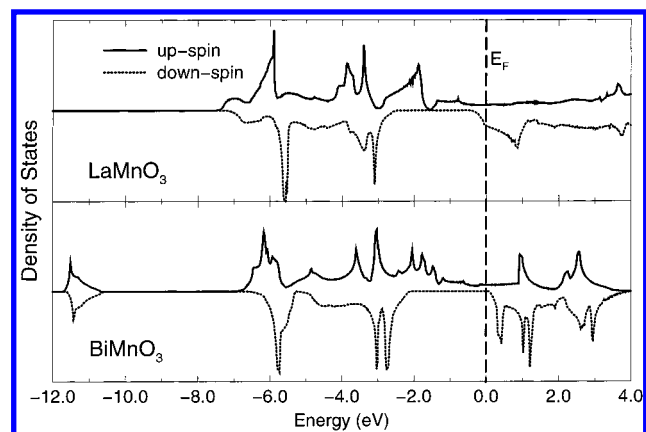
Feature Article

J. Phys. Chem. B, Vol. 104, No. 29, 2000 **6703**

Figure 12. Calculated densities of states for cubic ferromagnetic $LaMnO_3$ and $BiMnO_3$.

addition to their potential utility as multiferroic materials, Bi compounds provide the ability to tune the positions of phase boundaries by substitution of Bi for the rare earth ions, which might prove valuable in optimizing materials properties for specific device applications.

5.1.3. Cubic Ferromagnetic Structures. Next, we present the results of calculations in which the high-symmetry cubic structure is retained, but the electrons are allowed to spin polarize. We find that the introduction of spin polarization reduces the energy of both $BiMnO_3$ and $LaMnO_3$ by around 1 eV per unit cell compared with the paramagnetic case. The most important observation of this section is that the *differences* between $BiMnO_3$ and $LaMnO_3$ that we observed in the paramagnetic calculations persist into the ferromagnetic phase, with the PM to FM transition introducing the same kinds of changes in both materials.

Figure 12 shows the calculated densities of states for cubic ferromagnetic $LaMnO_3$ and $BiMnO_3$. The majority spins are represented by the solid line on the positive y axis, and the minority spins by the dotted line on the negative y axis. In both $LaMnO_3$ and $BiMnO_3$, the down-spin Mn 3d band is split off from the O 2p band and has a similar form to the corresponding paramagnetic band. The up-spin Mn 3d hybridizes strongly with the O 2p, and there is no band gap for the majority carriers. The up-spin DOS at the Fermi level in $LaMnO_3$ is still high, indicating that the cubic FM state has a high energy. This is consistent with the fact that the lowest-energy spin polarization in *structurally relaxed* $LaMnO_3$ is antiferromagnetic.[41] The DOS at the Fermi level in $BiMnO_3$ is somewhat lower, suggesting that the FM phase should be more stable in $BiMnO_3$ than in $LaMnO_3$. For both compounds, the Fermi level cuts through the very bottom of the down-spin Mn 3d bands, and the conduction band is occupied almost entirely by up-spin electrons. Again, the most obvious differences between the two electronic structures are the presence of the Bi 6s band between -10 and -12 eV and the contrasting forms of the Bi 6p and La 5d bands.

Figure 13 shows the up- and down-spin band structures for $BiMnO_3$ and $LaMnO_3$ along the high-symmetry axes of the simple cubic Brillouin zone. There are many similarities between the FM and PM energy bands, and our earlier conclusions regarding the origins of the differences between $BiMnO_3$ and $LaMnO_3$ continue to be valid. A detailed analysis of the band structures is presented in ref 36. Here, we summarize the important conclusions. First, the states that correspond to nonmagnetic orbitals (that is, the lower O 2p bands and the Bi 6s and La 5d bands) are unchanged from the paramagnetic state

and are identical for up- and down-spin electrons. Second, for both materials, the up-spin Mn 3d and O 2p bands are strongly hybridized, and there is no gap between them. However, the down-spin Mn 3d are split off from the O 2p bands by a larger gap than in the PM case. Finally, the $BiMnO_3$ minority conduction electrons have a large directional Bi 6p component, in striking contrast to those in $LaMnO_3$, in which the electrons are localized entirely in the Mn 3d orbitals. The fact that the conduction electrons partly occupy p-type atomic orbitals should produce quite different transport characteristics than those observed in conventional rare earth manganites, in which the conduction bands are entirely Mn 3d-type.

5.1.4. Soft-Mode Ferroelectric Distortions. Finally, we calculate the phonon modes in $BiMnO_3$ and $LaMnO_3$ to determine the existence and nature of ferroelectric instabilities. In keeping with the philosophy of this paper, we study the lattice distortions of the high-symmetry cubic phases and compare our results for $BiMnO_3$ with those for $LaMnO_3$. We restrict our discussion to zone-center phonons.

The perovskite manganites have 5 atoms per unit cell, which results in 15 phonon branches, 3 acoustical and 12 optical. At the Γ point, all phonons are 3-fold degenerate, so there is one acoustical phonon frequency (which is zero) and four optical frequencies. We are interested in the optical phonons that have negative eigenvalues, indicating lattice instabilities.

The force constant matrices for $LaMnO_3$ and $BiMnO_3$ were determined by calculating the Hellmann–Feynman forces resulting from the displacement of each atom in turn 0.1 Å along the z direction of the unit cell. The forces exerted on the Mn ions by the other ions were determined using the acoustic sum rule. We calculated the Mn–Mn force by applying the acoustic sum rule to both the columns and the rows of the resulting matrix. The two values differed by less than $\sim$0.001 eV/Å.

The paramagnetic cubic phases of both $LaMnO_3$ and $BiMnO_3$ have two unstable zone-center phonon modes. The frequencies and eigenvectors of the unstable modes are given in Table 3. The mode involving motion of the equatorial oxygens, shown in Figure 14b, does not correspond to a ferroelectric distortion and will not be discussed further. The displacement pattern for the second unstable mode is shown in Figure 14a. Here, the large (Bi or La) cations are moving in opposition to the oxygen cage, resulting in a ferroelectric displacement. The imaginary frequency of this mode is twice as large in $BiMnO_3$ than in $LaMnO_3$, indicating a stronger instability in the Bi compound. It is interesting to note that the Mn is moving in the same direction as the oxygen ions. This is opposite to the behavior of the Ti ion in $BaTiO_3$ and $PbTiO_3$, but similar to the behavior of Zr in $PbZrO_3$.[42]

In the ferromagnetic phase of $BiMnO_3$, the ferroelectric mode remains strongly unstable, at $82.30i$ cm^{-1}. However, he imaginary frequency phonons in the ferromagnetic phase of $LaMnO_3$ are considerably less unstable than the corresponding imaginary frequency paramagnetic phonons. In fact, the ferroelectric mode in $LaMnO_3$ is now only slightly unstable, at $21.1i$ cm^{-1}, and the other formerly unstable mode now has a positive frequency. Note, however, that the internal stresses are the same for the paramagnetic and ferromagnetic cubic phases in both materials. This weakening of the zone-center ferroelectric instability in $LaMnO_3$ is likely indicative of the tendency of the spin-polarized d^4 ion to Jahn–Teller distort in the absence of other bonding considerations.

It is clear from our analysis that the presence of ferroelectricity in $BiMnO_3$, and the absence of ferroelectricity in $LaMnO_3$, can be explained by the different zone-center lattice
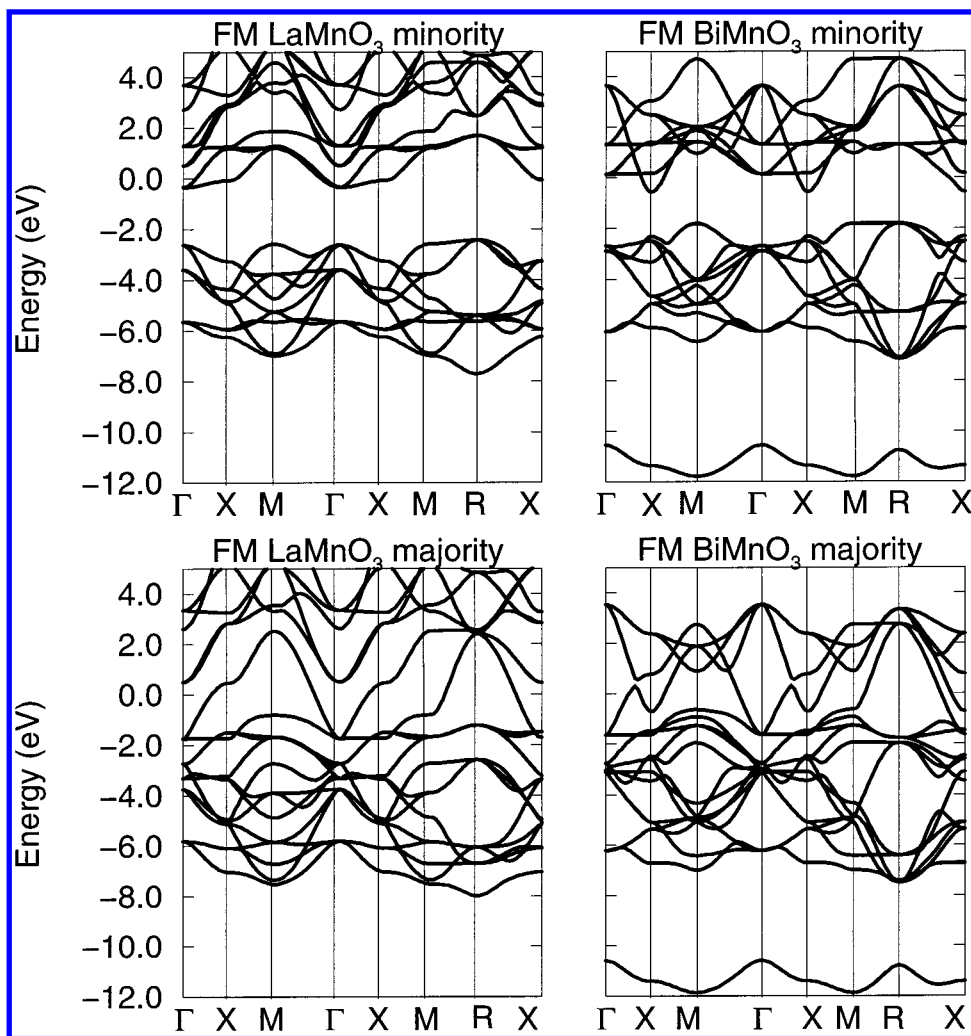
Figure 13. Up- and down-spin band structures for cubic LaMnO$_3$ and BiMnO$_3$ along the high-symmetry axes of the Brillouin zone.

TABLE 3: Eigenvectors and Eigenvalues of the Dynamical Matrix That Correspond to the Unstable Phonon Modes in Cubic Paramagnetic BiMnO$_3$ and LaMnO$_3$

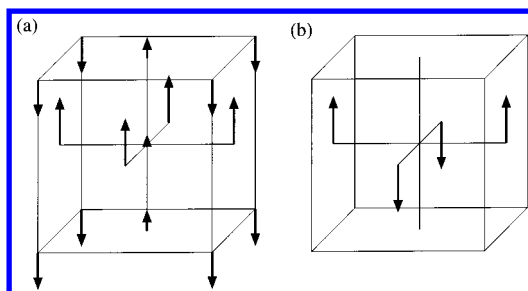| BiMnO$_3$						LaMnO$_3$					
ν (cm^{-1})	Bi	Mn	Oz	Ox	Oy	ν (cm^{-1})	La	Mn	Oz	Ox	Oy
72.39i	0.0	0.0	0.0	$-1/\sqrt{2}$	$1/\sqrt{2}$	49.04i	0.0	0.0	0.0	$-1/\sqrt{2}$	$1/\sqrt{2}$
98.20i	-0.43	0.09	0.16	0.62	0.62	44.69i	-0.59	0.22	0.21	0.53	0.53

Figure 14. (a) Eigenvector of the unstable ferroelectric Γ point phonon mode in BiMnO$_3$. The Mn ion is at the center of the unit cell surrounded by an octahedra of oxygens, with the large cations at the unit cell corners. (b) Nonferroelectric mode that is unstable in LaMnO$_3$. Each mode is 3-fold degenerate.

instabilities. Although a definitive prediction requires calculation of the phonon dispersion throughout the entire Brillouin zone, it is likely that the weakly unstable zone-center phonon in LaMnO$_3$ will be overshadowed by a stronger instability elsewhere in the Brillouin zone, reproducing theoretically the experimentally observed Jahn–Teller distortion. Similarly, the

very unstable ferroelectric mode at the zone center in BiMnO$_3$ is likely to dominate over possible unstable modes at other frequencies, confirming theoretically the suggested existence of ferroelectricity in BiMnO$_3$. This mode is driven by Bi–O covalency and creates a Bi–O electric dipole moment, in contrast to the conventional perovskite oxide ferroelectrics, in which B cation–oxygen covalency is the principal driving force for the ferroelectric distortion. Thus, we conclude that the d electron occupation on the manganese ion in BiMnO$_3$ continues to inhibit displacement of the B cation. It is only because of the unusual behavior of the A cation that ferroelectricity can occur at all.

5.1.5. Electronic Ferroelectricity. Ferroelectricity can also occur if the magnetic electronic state in the cubic phase (before the ferroelectric lattice distortion takes place) has a propensity to dipolar instability.[43] In this case, the driving mechanism for ferroelectricity is *electronic* instability,[43] rather than the usual softening of the phonon mode.[44,18] In these so-called "electronic ferroelectrics", the ferroelectric phase transition is driven by a change in the electronic structure rather than the crystal structure.

Feature Article

J. Phys. Chem. B, Vol. 104, No. 29, 2000 **6705**

(Of course electron−phonon coupling can cause a lattice distortion as a secondary effect of the transition, but a change in crystal structure is not required).

Electronic ferroelectricity has been demonstrated theoretically in the strongly correlated insulating phase of the Falicov−Kimball model, in which the Coulomb attraction between the localized f holes and itinerant d electrons leads to a built-in coherence between d and f states.[43] Subsequent Bose−Einstein condensation of d−f excitons, in which d and f states of opposite parity are paired, breaks the inversion symmetry of the underlying crystal. A requirement for the condensation is that the d−f Coulomb interaction dominates over the hybridization. The phase transition to the electronic ferroelectric state occurs when the d−f exciton energy goes to zero (instead of when a TO phonon frequency vanishes). Predicted values of the built-in polarization in an electronic ferroelectric are around 10 μC/cm^2, similar to the values found in perovskite ferroelectrics.

The results that we have obtained for BiMnO$_3$[36] suggest that electronic ferroelectricity might occur in this and other multiferroic materials. In the case of BiMnO$_3$, the localized state will be Mn 3d in origin, and the itinerant state will derive from Bi 6p. We observe a band crossing between the Bi 6p and Mn 3d bands of the same symmetry in the cubic phase, indicating zero hybridization between these orbitals. In addition, charge transfer occurs from a nominally occupied Mn 3d state into a Bi 6p band, resulting in an on-site d−p Coulomb interaction. Confirmation of the existence of electronic ferroelectricity will require further theoretical and experimental work.

5.1.6. Related BiBO$_3$ Materials. Our calculations have shown that a Bi A-site cation is favorable for ferroelectricity in perovskite oxides, regardless of whether the mechanism for ferroelectricity is electronic or soft-mode. Therefore, we anticipate that other Bi compounds will be good candidates for magnetoelectric multiferroism. BiFeO$_3$ is the only BiXO$_3$ compound (X = trivalent transition metal) that has been studied in any detail. It is known to be ferroelectric below 1110 K and antiferromagnetic with a Néel temperature of 670 K.[45] It shows the linear magnetoelectric effect, with applied magnetic fields inducing weak ferromagnetism and large increases in polarization.[46] Note that the Fe^{3+} ion in BiFeO$_3$ has the d^5 electron configuration and, therefore, is not a Jahn−Teller ion. BiCrO$_3$ (in which the Cr^{3+} ion has three d electrons) is also reported to be antiferromagnetic with a weak ferromagnetic moment,[35] but there have been no investigations (to our knowledge) of ferroelectricity. Little is known about BiCoO$_3$ and BiNiO$_3$ (d^6 and d^7 on the Co^{3+} and Ni^{3+} ions, respectively) beyond the fact that they have the cubic perovskite structure, but BiCo$_{0.5}$Fe$_{0.5}$O$_3$ is known to be ferromagnetic,[47] probably because of a double-exchange-type mechanism between neighboring d^6 and d^5 ions. We are beginning theoretical work on other Bi perovskite oxides with the hope that our results will stimulate experimental interest in these less-well-studied materials.

5.2. Yttrium Manganite. The literature on the hexagonal manganites is much more limited than that on the cubic perovskite manganites, and modern work focuses largely on yttrium manganite, YMnO$_3$. Although yttrium is not a rare earth element, it forms a stable trivalent cation with an ionic radius similar to those of the smaller rare earth ions. It is favored over the smaller rare earth ions in research studies for two reasons. First, a study of magnetic ordering on the Mn^{3+} ions is more straightforward in YMnO$_3$ than in the rare earth manganites as there is no perturbation from the rare earth f-electron magnetic moment. In addition, YMnO$_3$ forms in both the hexagonal and
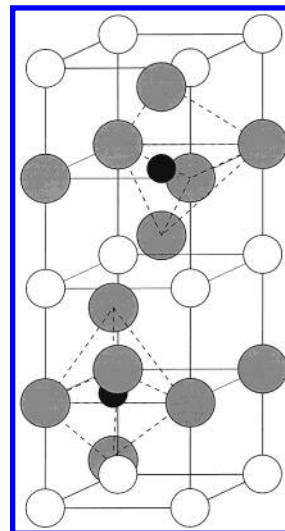

Figure 15. Hexagonal perovskite structure. The small B cation (in black) is 5-fold-coordinated by oxygen anions (in gray). The dashed lines indicate the oxygen pentahedra. The large A cations (white) occupy 7-fold-coordinated sites.

orthorhombic phases on solution synthesis at ambient pressure,[48] making it particularly appealing for use in a comparative study.

In this section, we compare the electronic properties of YMnO$_3$ in its high-pressure cubic perovskite structure with those of the prototypical cubic manganite, LaMnO$_3$. The purpose of our calculations is to determine the factors that make the cubic structure unstable, leading to stabilization of the hexagonal ferroelectric structure. In particular, by analogy with our results for BiMnO$_3$, we investigate whether involvement of the large cation (Y^{3+} in this case) in covalent bonding contributes to the stabilization of the ferroelectric phase. We begin by calculating the electronic structure without including magnetic effects, and then lower the magnetic symmetry to the ferromagnetic phase. Our calculations are performed at the experimental lattice constants of 3.95 Å for LaMnO$_3$ and 3.84 for YMnO$_3$.

5.2.1. Summary of Experimental Results. Early (1960s) work on YMnO$_3$[48] established the hexagonal phase to be ferroelectric, with the hexagonal perovskite structure and the *P6$_3$cm* space group. The hexagonal perovskite structure consists of ABC ACB... stacking of close packed O layers, with the Mn ions occupying 5-fold-coordinated sites and the rare earth atoms in 7-fold-coordinated interstices. The ideal high-temperature paraelectric structure consists of two formula units per unit cell and is shown in Figure 15. Because this structure does not occur in the perovskite ferrites, it has been suggested that the ability of Mn^{3+} to form 5-fold trigonal bipyramids through dsp^3 hybrid bonding is a requirement.[48] Early reports of a weak parasitic ferromagnetism[49] were soon shown to be the result of Mn$_3$O$_4$ impurity contaminating the powdered phase,[50] and weak ferromagnetism was shown to be absent in single-crystal samples.[50]

In the 1970s, work began on the orthorhombic phase. Susceptibility measurements established that orthorhombic YMnO$_3$ is an antiferromagnet with a Néel temperature of 42 K, although significant deviations from Curie−Weiss behavior were seen well above the manganese ordering temperature.[51] A more detailed study[52] concluded that the Mn^{3+} ordering is helical with a propagation wavevector **k** = [0, 0.0786, 0] and a helical angle from plane to plane of 14°. Within each plane the ordering is A-type antiferromagnetic. Modern studies of hexagonal YMnO$_3$ have revealed a coupling between the ferroelectric and magnetic ordering.[34] Although the ferroelectric Curie temperature (914 K) is quite different from the Néel
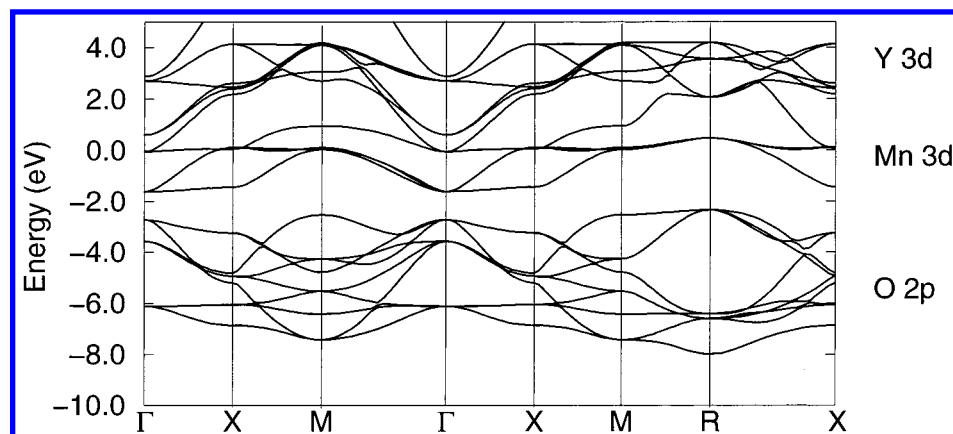
Figure 16. Calculated band structures for cubic paramagnetic YMnO$_3$ along the high-symmetry axes of the Brillouin zone.

temperature (80 K), anomalies in the dielectric constant and loss tangent near the Néel temperature are indicative of coupling between the ferroelectric and antiferromagnetic orders. The coupling has been attributed to changes in the phonon spectrum associated with the antiferromagnetic transition.[34] Raman and infrared spectroscopy of the high-temperature paraelectric and low-temperature ferroelectric phases show only weak bands in the ferroelectric phase because of the noncentrosymmetricity. This indicates that the structural differences between the ferroelectric and paraelectric phases are very small. Nonlinear optical spectroscopy[53] shows two types of optical second-harmonic spectra of the Mn^{3+} ions in hexagonal YMnO$_3$, one from the noncentrosymmetric ferroelectric ordering of charges and the other from the centrosymmetric antiferromagnetic ordering of spins. Partial overlapping between the electronic transitions results in a nonlinear optical polarization that depends on two order parameters. A generalized Ginzburg–Landau formalism has been developed, which shows that the second-harmonic generation susceptibility is directly proportional to the bilinear combination of both order parameters.[54] Finally, epitaxial thin films of hexagonal YMnO$_3$ have been grown on MgO(111) and ZnO/Al(0001)[55] and explored for use as non-volatile memory devices.

There has also been some modern work on the orthorhombic phase of YMnO$_3$. Attempts have been made to find a synthesis that will produce a larger proportion of the metastable orthorhombic phase.[56] In addition, the Raman spectrum of orthorhombic YMnO$_3$ has been measured, and the Raman active phonon modes determined and compared with those of LaMnO$_3$.[57]

5.2.2. Cubic Paramagnetic Structures. First, we present results for YMnO$_3$ in the cubic paramagnetic phase and compare them with our earlier results for LaMnO$_3$. Figure 16 shows the calculated band structure of cubic paramagnetic YMnO$_3$, plotted along the high-symmetry axes of the cubic Brillouin zone. The plotted energy range is from −10 to 5 eV, and the lower-lying semi-core states have been omitted for clarity. The Fermi level is set to zero. As in LaMnO$_3$, the broad series of bands between approximately −2 and −7 eV arises from the oxygen 2p orbitals. Above the oxygen 2p bands, and separated from them by an energy gap, are the Mn 3d bands. The Mn 3d bands are slightly broader than those in LaMnO$_3$ because the smaller lattice constant results in greater Mn 3d–O 2p overlap. As in LaMnO$_3$, the Mn 3d bands are divided into two subbands—the lower energy t$_{2g}$ bands and the higher energy e$_g$ bands—as a result of crystal-field splitting by the octahedral oxygen anions. The Fermi level lies near the top of the Mn 3d t$_{2g}$ bands and is in a region of high density of states, suggesting that a lower-energy

structure could be achieved by allowing spin polarization and/or structural distortion. In LaMnO$_3$, the Mn 3d bands were largely separated in energy at each *k* point from the next-highest-energy La 5d bands. The Y 4d bands are slightly lower in energy than the La 5d bands, resulting in a small amount of overlap with the top of the Mn 3d bands. This occurs at around 3 eV above the Fermi energy, however, and is unlikely to have a strong effect on structural stability or transport properties.

Again, to quantify the interactions in YMnO$_3$, we perform a tight-binding analysis of the band structure and compare our results with those obtained in section 5.1 for LaMnO$_3$. The similarities between LaMnO$_3$ and YMnO$_3$ are particularly striking along the Γ → X line. This region of the band structure is shown in Figure 17, with the symmetry labels added and the energy scale extended to include the lower-energy O 2s and La 5p bands. For clarity, the Δ_1 bands are plotted with solid lines, all other bands are plotted with dashed lines, and the symmetry labels are written next to the line. The behavior of the bands in YMnO$_3$ is similar to that of the corresponding bands in LaMnO$_3$. In both cases, the oxygen 2p Δ_1 bands decrease monotonically in energy from Γ to X, and the Mn 3d Δ_1 band increases monotonically from Γ to X. Also, in both cases, the lowest-energy O 2p Δ_5 band is approximately constant in energy, whereas the higher-energy O 2p Δ_5 bands decrease monotonically and the Mn 3d Δ_5 bands increase monotonically. Both the O 2s and 2p Δ_2 bands decrease monotonically along Γ to X, and one of the Mn 3d Δ_2 bands is constant, while the other increases in energy. All Δ_2' bands are approximately constant in energy.

As in the case of LaMnO$_3$, a good fit (RMS deviation = 0.2) is obtained using only the Mn 3d, O 2s, and O 2p orbitals in the basis. The tight-binding parameters that we obtained by nonlinear least-squares fitting[37] to the calculated ab initio energies at 21 points along the Γ to X axis are given in Table 1. The parameters for YMnO$_3$ are similar to those for LaMnO$_3$, except for an increase of around 10% in the Mn 3d–O nearest-neighbor overlaps. This is a consequence of the smaller lattice constant in YMnO$_3$ and results in the slightly broader Mn 3d bands noted above.

The results of our tight-binding analysis indicate that there is no significant covalent bonding between the Y 4d orbitals and either the oxygen 2p or the Mn 3d orbitals. We anticipate a similar situation in the smaller rare earth manganites, although the situation might be complicated slightly by the lanthanide contraction, which should cause the 5d orbital energies to be lowered into the energy range of the Mn 3d orbitals, with a resulting decrease in ionic character.[58] Therefore, we conjecture that the observed differences between the properties of hex-
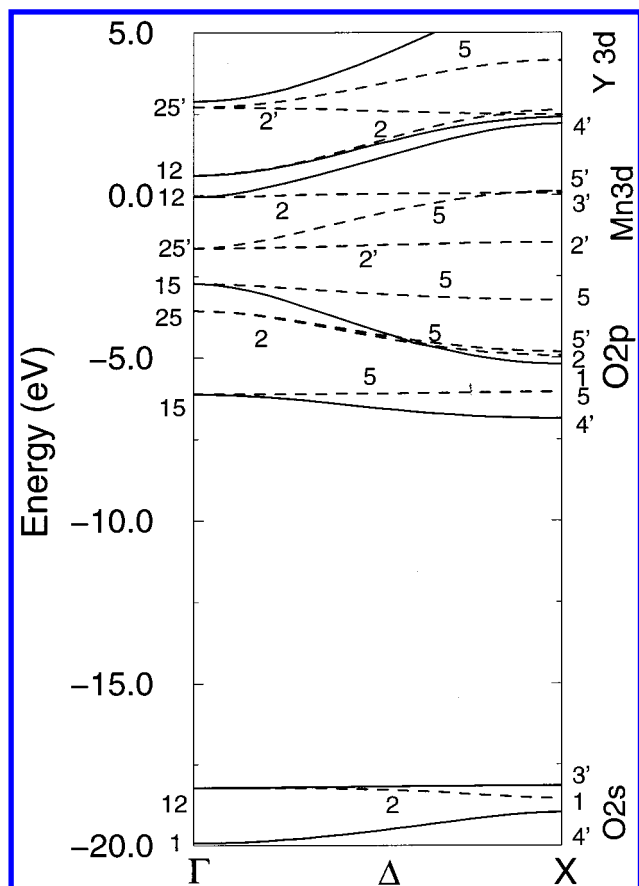
Feature Article

J. Phys. Chem. B, Vol. 104, No. 29, 2000 **6707**

Figure 17. Calculated band structures for cubic paramagnetic YMnO₃ along the Γ → X axis. The solid lines show the bands of Δ_1 symmetry. The numbers indicate the symmetry types of the other lines and points.

Figure 18. Up- and down-spin band structures for cubic ferromagnetic YMnO₃ along the high-symmetry axes of the Brillouin zone.

agonal and cubic manganites are merely the result of the different sizes of the large cations in the two materials and are not due to any additional covalent bonding effects.

5.2.3. Cubic Ferromagnetic Structures. As in the case of BiMnO₃ and LaMnO₃, the differences and similarities between YMnO₃ and LaMnO₃ that we observed in the paramagnetic calculations persist into the ferromagnetic phase, with the PM to FM transition introducing the same kinds of changes in both materials. We find that the introduction of spin polarization reduces the energy of YMnO₃ by ∼0.7 eV compared with the PM phase, slightly less than both BiMnO₃ and LaMnO₃, which were stabilized by ∼1 eV.

Figure 18 shows the calculated up- and down-spin band structures for YMnO₃ along the high-symmetry axes of the simple cubic Brillouin zone. There are many similarities between the FM and PM energy bands, and our earlier conclusions regarding the differences and similarities between YMnO₃ and LaMnO₃ continue to be valid. The down-spin Mn 3d band in FM YMnO₃ is split off from the O 2p band and has a form similar to that of the corresponding bands in PM YMnO₃ and in PM and FM LaMnO₃. The hybridization between up-spin Mn 3d electrons and oxygen remains weak in YMnO₃, and the Mn 3d band remains split off from the O 2p band. This is in contrast to LaMnO₃, for which the majority Mn 3d band mixes strongly with the O 2p band. As a result, the O 2p bands in YMnO₃ are identical for up and down spin. In contrast, in LaMnO₃ the higher O 2p bands are strongly hybridized with the Mn 3d bands and, therefore, show a polarization dependence. The Y 4d bands are largely spin-independent, although the minority Y 4d bands are at a slightly higher energy than the majority bands. Finally, the Fermi level in YMnO₃ is in a region
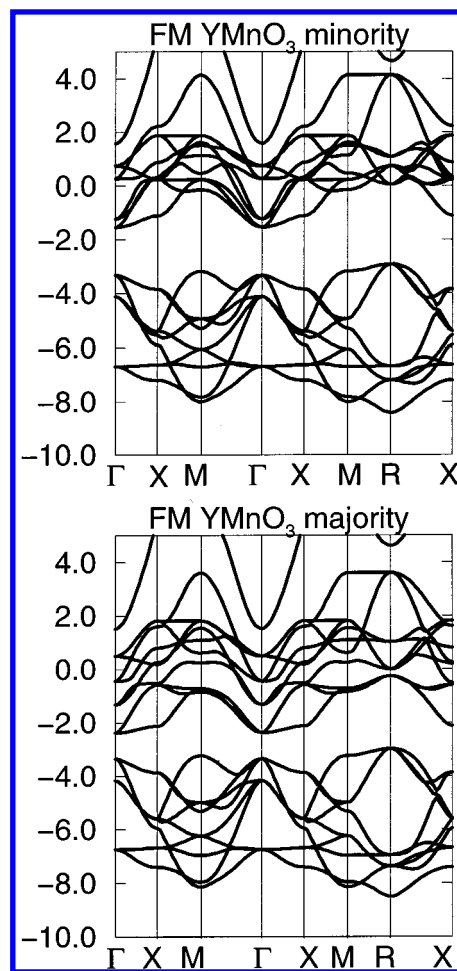
of high density of states for both up- and down-spin bands, indicating that cubic YMnO₃ is not a half-metallic material.

5.2.4. Conclusions for YMnO₃. In conclusion, our results indicate that the interaction between the Y 4d and O 2p atomic orbitals in YMnO₃ is largely ionic in character. This is in contrast to BiMnO₃, which has strong Bi−O covalency, but is analogous to LaMnO₃, in which the La 5d−O 2p is largely ionic in character. Therefore, we suggest that the stabilization of different structural phases in LaMnO₃ and YMnO₃ is driven purely by the different sizes of the La and Y cations. This is consistent with the previously held view that the formation of a cubic or hexagonal manganite is determined by the size of the large cation. The small size of the yttrium ion is then indirectly responsible for the ferroelectricity in YMnO₃, which is the result of the unusual 5-fold coordination around the Mn ion in the hexagonal structure removing the center of symmetry and creating an electric dipole moment.

6. Summary and Future Work

In summary, we have presented an overview of the field of multiferroic magnetoelectric materials and a detailed study of two magnetically ordered ferroelectrics. In the course of our discussion, a ferroelectric "d⁰" rule has emerged, that is, a ferroelectric displacement of the B cation in perovskite oxides is inhibited if the formal charge does not correspond to a d⁰ electron configuration. We have seen that this d⁰ rule can be broken, providing the potential for simultaneous magnetic and ferroelectric ordering, if details of chemistry or structure create an asymmetric potential with a double potential well *in spite* of

the d occupation of the magnetic cation. In the antiferromagnetic ferroelectric manganites of Y and the small rare earth elements, the double potential well is created by the 5-fold oxygen coordination. In $BiMnO_3$ (and also possibly in $BiFeO_3$), the asymmetry is created by the Bi−O hybridization. Also, in the classic example of nickel iodine boracite, $Ni_3B_7O_{13}I$, the anisotropic iodine−oxygen octahedron is believed to cause an electrostatic double potential well along the I−Ni−I axis. [Note, however, that experiments on materials including $BaCr(O_2F)$, $BaFe(O_2F)$, $PbCr(O_2F)$ and $PbFe(O_2F)$, in which asymmetry was sought by replacing part of the oxygen octahedron with fluorine, have not been successful in producing ferromagnetic ferroelectrics.[59]]

The fundamental theoretical question of if (and why) d^0-ness is so strongly favored remains to be answered rigorously and will undoubtedly contribute significantly to the future understanding of both ordinary ferroelectrics and of multiferroic materials. However, the existence of a Jahn−Teller distortion seems to be particularly unfavorable; therefore, we propose that non-Jahn−Teller ions are more likely candidates for magnetic ferroelectric ions.

There has been little modern experimental work on magnetic ferroelectrics, and the synthesis of single crystals of known or candidate multiferroic materials will be essential in elucidating the nature of the interactions involved. We hope that this paper will stimulate experimental work on some of the less well studied, but potentially interesting, candidate multiferroic materials. In particular, this paper has focused exclusively on oxide ferroelectrics; however, non-oxide-based ferroelectrics should also be considered as candidates for multiferroism. In ferroelectrics such as $NaCaF_3$, the driving force for ferroelectricity is Coulomb interactions, rather than covalency. This might allow circumvention of the d^0 requirement, provided that suitable stable structures can be found.

Appendix: Computational Techniques Used in this Work

The calculations described in this work were performed using a plane-wave pseudopotential (PWPP) implementation[60] of density functional theory (DFT)[61] within the local spin density approximation (LSDA). The accuracy and efficiency of ab initio pseudopotential calculations (compared with all-electron calculations) has long been established for *nonmagnetic* systems[62] and has recently been verified for spin-polarized *magnetic* systems. [Traditionally, magnetic materials containing transition metals have been studied using all-electron methods with mixed basis sets, such as the linear-augmented plane wave (LAPW),[63] linear muffin-tin orbital,[64] or Korringa−Kohn−Rostoker[65] approaches.]

A.1. Application of the Plane-Wave Pseudopotential Method to Magnetic Materials. Resistance to the use of the PWPP method to study magnetic systems was based on two perceived difficulties. First, the magnetic properties of the transition metals and their compounds originate from tightly bound d-electrons, which were believed to require a prohibitively large number of plane waves to expand their pseudopotentials. In this work, we use the optimized pseudopotentials developed by Rappe et al.[66] to reduce the energy cutoff of the plane-wave expansion to

around 60 Ry. Second, implicit within the pseudopotential approximation is the assumption that the exchange−correlation potential, V_{xc}, is separable into a valence part and a core part.

$$V_{xc}(\rho,\sigma) = [V_{xc}(\rho,\sigma) - V_{xc}(\rho^v,\sigma^v)] + V_{xc}(\rho^v,\sigma^v) \quad (2)$$

Here, ρ is the electron density, σ is the spin polarization, and the superscript v refers to the contribution from the valence electrons. This separation is only rigorously correct if the core electrons are spatially separated from the valence electrons, which is not true for transition metal ions. Here, we circumvent this problem using the partial nonlinear core correction scheme of Louie et al.,[67] in which the core charge density is explicitly retained both in the construction of the ionic pseudopotential and in the DFT calculation.

The PWPP method with optimized pseudopotentials and partial nonlinear core corrections was first tested by Sasaki et al. for ferromagnetic nickel and iron.[68] The structural and magnetic properties calculated using the PWPP method were found to be in excellent agreement with results from all-electron calculations. A similar study using different soft pseudopotentials obtained comparable results for the ground-state properties of nickel.[69] More recently, Lewis and co-workers presented the first PWPP calculation for a magnetic *compound* (CrO_2)[70] and showed that the results agreed well with those of all-electron LSDA calculations. It has also been shown to give results in agreement with those of published all-electron calculations[71] for magnetic perovskites related to those studied in this work.[36]

A.2. Pseudopotential Construction. For La, Bi, and Y, we constructed optimized scalar-relativistic pseudopotentials, using (for La) a $5s^25p^65d^1$ reference configuration with core radii $r_c = 2.6$ au for all orbitals, and (for Y) a $4s^24p^64d^1$ reference configuration with $r_c(s) = r_c(d) = 1.5$ au and $r_c(p) = 1.6$ au. Neither La nor Y have 4f orbitals in their reference configuration, which facilitates the application of the pseudopotential method. The pseudopotentials were optimized using four basis functions per orbital, with cutoff wavevectors, q_c, of 7.5 au. q_c determines the convergence of the kinetic energy with respect to the plane-wave cutoff energy in reciprocal-space calculations. For Mn and O, we constructed nonrelativistic optimized pseudopotentials. The oxygen pseudopotentials were generated from a $2s^22p^4$ reference configuration with core radii of 1.5 au for both the s and the p orbitals. They were then optimized using four and three basis functions with q_c of 7.0 and 6.5 au for s and p orbitals, respectively. The oxygen pseudopotentials were used successfully in earlier calculations for nonmagnetic perovskite oxides.[44] For Mn, a $4s^{0.75}4p^{0.25}3d^5$ reference configuration was used, with r_c equal to 2.0, 2.15, and 2.0 au for s, p, and d orbitals, respectively. The optimized pseudopotentials for Mn were constructed using four basis functions and $q_c = 7.5$ au, and partial nonlinear core corrections[67] were included. The core charge was approximated by a zeroth-order spherical Bessel function within a radius of 0.737 au, with the full core charge used outside this radius. The pseudopotentials were tested for transferability by comparing with all-electron calculations for a range of typical atomic and ionic configurations. The pseudo-eigenvalues and total energies were found to be equivalent to the all-electron values to within a few millielectronvolts. Plots of all pseudopotentials have been shown in earlier publications.[36,72]

All pseudopotentials were put into separable form[73] using two projectors for each angular momentum.[74] The first projector was taken as the atomic pseudo wave function, and the second projector as r^2 times the first projector, suitably orthogonalized to the first.[75] For La, Y, and Mn, the $l = 0$ component was chosen as the local potential. For oxygen, the local potential was the l

= 1 component. The absence of ghost states was confirmed using the ghost theorem of Gonze, Käckell, and Scheffler.[76]

A.3. Technical Details. The total energy and band structure calculations were performed on Silicon Graphics Power Challenge L and O2 workstations using the conjugate gradient program CASTEP 2.1,[77,78] which we have extended to study spin-polarized systems. We used a plane-wave cut off of 60 ry, which corresponds to about 3500 plane waves in a cubic unit cell with a lattice constant of $\sim$4 Å. A variable Gaussian broadening between 1 and 0.002 eV was applied to the k-point sampling to speed convergence for metallic systems. A $6 \times 6 \times 6$ Monkhorst-Pack[79] grid was used for all calculations for cubic systems. This led to 10 k points in the irreducible Brillouin zone for the high-symmetry cubic structures and a correspondingly higher number for the distorted structures with lower symmetry. The exchange correlation was calculated using the Perdew−Zunger parametrization[80] of the Ceperley−Alder potential[81] with the von Barth−Hedin interpolation formula.[82] For density of states calculations, we interpolated the calculated eigenvalues to a grid of $\sim$350,000 k points in the irreducible simple cubic Brillouin zone using the interpolation scheme of Monkhorst and Pack.[79] We then applied the Gilat−Raubenheimer method[83] to integrate over this fine mesh.

References and Notes

(1) Pockels, F. *Abh. Gött* **1894**, *39*, 1.

(2) Valasek, J. *Phys. Rev.* **1921**, *17*, 475.

(3) Mueller, H. *Phys. Rev.* **1940**, *57*, 829.

(4) Busch, G.; Scherrer, P. *Naturwissenschaften* **1935**, *23*, 737.

(5) Slater, J. C. *J. Chem. Phys.* **1941**, *9*, 16.

(6) von Hippel, A.; Breckenridge, R. G.; Chesley, F. G.; Tisza, L. *Ind. Eng. Chem. Res.* **1946**, *38*, 1097.

(7) Cohen, R. E. *J. Phys. Chem. Sol.* **2000**, *61*, 139−146.

(8) Simonds, J. L. *Phys. Today* **1995**, April, 26−32.

(9) See, for example: *Phys. Today* **1995**, April and references therein.

(10) Baibich, M. N.; Broto, J. M.; Fert, A.; Nguyen Van Dau, F.; Petroff, F.; Etienne, P.; Creuzet, G.; Friederich, A.; Chazelas, J. *Phys. Rev. Lett.* **1988**, *61*, 2472−2475.

(11) Jin, S.; Tiefel, T. H.; McCormack, M.; Fastnacht, R. A.; Ramesh, R.; Chen, L. H. *Science* **1994**, *264*, 413.

(12) Johnson, M. *IEEE Spectrum* **1994**, May, 47.

(13) Sham, L. J. *J. Magn. Magn. Mater.* **1999**, *200*, 219.

(14) Wood, V. E.; Austin, A. E. In *Magnetoelectric Interaction Phenomena in Crystals*; Freeman, A. J., Schmid, H., Eds.; Gordon and Breach: Newark, NJ, 1975.

(15) Weiss, P. *J. Phys.* **1907**, *6*, 661.

(16) Stoner, E. C. *Philos. Mag.* **1933**, *15*, 1080.

(17) Cross, L. E. *Mater. Chem. Phys.* **1996**, *43*, 108−15.

(18) Cohen, R. E.; Krakauer, H. *Ferroelectrics* **1992**, *136*, 95.

(19) Schmid, H. *Ferroelectrics* **1994**, *162*, 317.

(20) Ascher, E.; Rieder, H.; Schmid, H.; Stössel, H. *J. Appl. Phys.* **1966**, *37*, 1404.

(21) Smolensky, G. A.; Agranovskaya, A. I.; Isupov, V. A. *Sov. Phys. Solid State* **1959**, *1*, 149.

(22) Smolensky, G. A.; Isupov, V. A.; Krainik, N. N.; Agranovskaya, A. I. *Isvest. Akad. Nauk SSSR, Ser. Fiz* **1961**, *25*, 1333.

(23) Brixel, W.; Rivera, J.-P.; Steiner, A.; Schmid, H. *Ferroelectrics* **1988**, *79*, 201.

(24) Astrov, D. N.; Al'shin, B. I.; Tomashpol'skii, Y. Y.; Venevtsev, Y. N. *Sov. Phys. JETP* **1969**, *28*, 1123.

(25) Drobyshev, L. A.; Al'shin, B. I.; Tomashpol'skii, Y. Y.; Venevtsev, Y. N. *Sov. Phys. Cryst.* **1970**, *14*, 634.

(26) Shannon, R. D. *Acta Crystallogr.* **1976**, *A32*, 751.

(27) Mizokawa, T.; Khomskii, D. I.; Sawatzky, G. A. *Phys. Rev. B* **1999**, *60*, 7309.

(28) See, for example: Proceedings of the 41st Annual Conference on Magnetism and Magnetic Materials, Atlanta, GA, 1996 (*J. Appl. Phys.* **1997**, *81*, 8) and references therein.

(29) Asamitsu, A.; Moritomo, Y.; Tomioka, Y.; Arima, L.; Tokura, Y. *Nature* **1995**, *373*, 407.

(30) Kuwahara, H.; Tomioka, Y.; Asamitsu, A.; Moritomo, Y.; Tokura, Y. *Science* **1995**, *270*, 961.

(31) Brug, J. A.; Anthony, T. C.; Nickel, J. H. *MRS Bull.* **1996**, *21* (9), 23.

(32) Kuwahara, H.; Tomioka, Y.; Moritomo, Y.; Asamitsu, A.; Kasai, M.; Kumai, R.; Tokura, Y. *Science* **1996**, *272*, 80.

(33) Goodenough, J. B. *Phys. Rev.* **1955**, *100*, 564.

(34) Huang, Z. J.; Cao, Y.; Sun, Y. Y.; Xue, Y. Y.; Chu, C. W. *Phys. Rev. B* **1997**, *56*, 2623.

(35) Literature searches for 1960 and later turned up only the following five papers: Troyanchuk, I. O. et al. *JETP* **1994**, *78*, 212. Troyanchuk, I. O. et al. *Sov. Phys. Solid State* **1990**, *32*, 1436. Tomashpol'skii, Y. Y. et al. *Sov. Phys. Cryst.* **1972**, *16*, 905. Bokov, V. A. et al. *Bull. Acad. Sci. USSR* **1969**, *33*, 182. Sugawara, F. et al. *J. Phys. Soc. Jpn.* **1968**, *25*, 1553.

(36) Hill, N. A.; Rabe, K. M. *Phys. Rev. B* **1999**, *59*, 8759.

(37) Mattheiss, L. F. *Phys. Rev. B* **1972**, *6*, 4718.

(38) Rao, C. N. R.; Arulraj, A.; Cheetham, A. K.; Raveau, B. *J. Phys.: Condens. Matter* **2000**, *12*, R83−R106.

(39) Bao, W.; Axe, J. D.; Chen, C. H.; Cheong, S.-W. *Phys. Rev. Lett.* **1997**, *78*, 543.

(40) Schiffer, P.; Ramirez, A. P.; Bao, W.; Cheong, S.-W. *Phys. Rev. Lett.* **1995**, *75*, 3336.

(41) Wollan, E. O.; Koehler, W. C. *Phys. Rev.* **1955**, *100*, 545.

(42) Ghosez, Ph.; Cockayne, E.; Waghmare, U. V.; Rabe, K. M. *Phys. Rev. B* **1999**, *60*, 836−843.

(43) Portengen, T.; Östreich, Th.; Sham, L. J. *Phys. Rev. Lett.* **1996**, *76*, 3384−3387; *Phys. Rev. B* **1996**, *54*, 17452−17463.

(44) Waghmare, U. V.; Rabe, K. M. *Phys. Rev. B* **1997**, *55*, 6161.

(45) Sosnowska, I.; Neumaier, T. P.; Steichele, E. *J. Phys. C* **1982**, *15*, 4835−4839.

(46) Popov, Y. F.; Zvezdin, A. K.; Vorob'ev, G. P.; Kadomtseva, A. M.; Murashev, V. A.; Rakov, D. N. *JETP Lett.* **1993**, *57*, 69−71.

(47) Vasudevan, S.; Rao, C. N. R.; Umarji, A. M.; Subba Rao, G. V. *Mater. Res. Bull.* **1979**, *14*, 451−454.

(48) Yakel, H. L.; Koehler, W. C.; Bertaut, E. F.; Forrat, E. F. *Acta Crystallogr.* **1963**, *16*, 957.

(49) Bertaut, E. F.; Pauthenet, R.; Mercier, M. *Phys. Lett.* **1963**, *7*, 110.

(50) Bertaut, E. F.; Pauthenet, R.; Mercier, M. *Phys. Lett.* **1965**, *18*, 13.

(51) Wood, W. E.; Austin, A. E.; Collins, E. W.; Brog, K. C. *J. Phys. Chem. Solids* **1973**, *34*, 859.

(52) Quezel, S.; Rossat-Mignod, J.; Bertaut, E. F. *Solid State Commun.* **1974**, *14*, 941.

(53) Fröhlich, D.; Leute, St.; Pavlov, V. V.; Pisarev, R. V. *Phys. Rev. Lett.* **1998**, *81*, 3239.

(54) Sa, D.; Valentí, R.; Gros, C. cond-mat/9910283, *Eur. J. Phys. B*, accepted.

(55) Fujimura, N.; Ishida, T.; Yoshimura, T.; Ito, T. *Appl. Phys. Lett.* **1996**, *69*, 1011.

(56) Brinks, H. W.; Fjellvåag, H.; Kjekshus, A. *J. Solid State Chem.* **1997**, *129*, 334.

(57) Iliev, M. N.; Abrashev, M. V.; Lee, H.-G.; Popov, V. N.; Sun, Y. Y.; Thomsen, C.; Meng, R. L.; Chu, C. W. *Phys. Rev. B* **1998**, *57*, 2872.

(58) Moeller, T. *The Chemistry of the Lanthanides*; Pergamon Press: Oxford, U.K., 1973.

(59) Schmid, H. In *Magnetoelectric Interaction Phenomena in Crystals*; Freeman, A. J., Schmid, H., Eds.; Gordon and Breach: Newark, NJ, 1975.

(60) Yin, M. T.; Cohen, M. L. *Phys. Rev. B* **1982**, *26*, 5668.

(61) Hohenberg, H.; Kohn, W. *Phys. Rev.* **1964**, *136*, 864. Kohn, W.; Sham, L. J. *Phys. Rev.* **1965**, *140*, 1133.

(62) See, for example: Cohen, M. L. *Phys. Today* **1979**, *32* (7), 40 and references therein.

(63) Singh, D. J. *Planewaves, Pseudopotentials and the LAPW Method*; Kluwer Academic Publishers: Dordrecht, The Netherlands, 1994.

(64) Anderson, O. K. *Phys. Rev. B* **1975**, *12*, 3060.

(65) Korringa, J. *Physica* **1947**, *13*, 392. Kohn, W.; Rostocker, N. *Phys. Rev.* **1954**, *94*, 1111.

(66) Rappe, A. M.; Rabe, K. M.; Kaxiras, E.; Joannopolous, J. D. *Phys. Rev. B* **1990**, *41*, 1227.

(67) Louie, S. G.; Froyen, S.; Cohen, M. L. *Phys. Rev. B* **1982**, *26*, 1738.

(68) Sasaki, T.; Rappe, A. M.; Louie, S. G. *Phys. Rev. B* **1995**, *52*, 12760.

(69) Cho, J.-H.; Kang, M.-H. *Phys. Rev. B* **1995**, *52*, 9159.

(70) Lewis, S. P.; Allen, P. B.; Sasaki, T. *Phys. Rev. B* **1997**, *55*, 10253.

(71) Pickett, W. E.; Singh, D. J. *Phys. Rev. B* **1996**, *53*, 1146.

(72) Hill, N. A. *J. Magn. Magn. Mater.*, submitted.

(73) Kleinman, L.; Bylander, D. M. *Phys. Rev. Lett.* **1982**, *48*, 1425.

(74) Blöchl, P. E. *Phys. Rev. B* **1990**, *41*, 5414.

(75) Teter, M. P. *Phys. Rev. B* **1993**, *48*, 5031.

(76) Gonze, X.; Käckell, P.; Scheffler, M. *Phys. Rev. B* **1990**, *41*, 12264.

(77) Payne, M. C.; Teter, M. P.; Allan, D. C.; Arias, T. A.; Joannopoulos, J. D. *Rev. Mod. Phys.* **1992**, *64*, 1045.

(78) Payne, M. C.; Weng, X.; Hammer, B.; Francis, G.; Bertram, U.; de Vita, A.; Lin, J. S.; Milman, V.; Qteish, A. Unpublished work.

(79) Monkhorst, H. J.; Pack, J. D. *Phys. Rev. B* **1976**, *13*, 5188.

(80) Perdew, J.; Zunger, A. *Phys. Rev. B* **1981**, *23*, 5048.

(81) Ceperley, D. M.; Alder, B. J. *Phys. Rev. Lett.* **1980**, *45*, 566.

(82) von Barth, U.; Hedin, L. *J. Phys. C* **1972**, *5*, 1629.

(83) Gilat, G.; Raubenheimer, L. C. *Phys. Rev.* **1966**, *144*, 390.